Size and Shape Constraints of (486958) Arrokoth from Stellar Occultations

Marc W. Buie[1], Simon B. Porter[1], Peter Tamblyn[1], Dirk Terrell[1], Alex Harrison Parker[1], David Baratoux[2], Maram Kaire[3,4], Rodrigo Leiva[1], Anne J. Verbiscer[5], Amanda M. Zangari[1], François Colas[6,7], Baïdy Demba Diop[8], Joseph I. Samaniego[9], Lawrence H. Wasserman[10], Susan D. Benecchi[11], Amir Caspi[1], Stephen Gwyn[12], J. J. Kavelaars[12], Adriana C. Ocampo Uría[13], Jorge Rabassa[14], M. F. Skrutskie[5], Alejandro Soto[1], Paolo Tanga[15], Eliot F. Young[1], S. Alan Stern[1], Bridget C. Andersen[5], Mauricio E. Arango Pérez[16], Anicia Arredondo[17], Rodolfo Alfredo Artola[18], Abdoulaye Bâ[19], Romuald Ballet[20,21], Ted Blank[22], Cheikh Tidiane Bop[19], Amanda S. Bosh[10,17], Matías Aarón Camino López[23,24], Christian M. Carter[9], J. H. Castro-Chacón[25], Alfonso Caycedo Desprez[26], Nicolás Caycedo Guerra[26], Steven J. Conard[22,27], Jean-Luc Dauvergne[28], Bryan Dean[29], Michelle Dean[29], Josselin Desmars[30], Abdou Lahat Dieng[19], Mame Diarra Bousso Dieng[19,31], Omar Diouf[4], Gualbert Séraphin Dorego[32,33], David W. Dunham[22,34], Joan Dunham[22], Hugo A. Durantini Luca[18], Patrick Edwards[5], Nicolas Erasmus[36], Gayane Faye[19], Mactar Faye[37], Lucas Ezequiel Ferrario[35], Chelsea L. Ferrell[1], Tiffany J. Finley[1], Wesley C. Fraser[38], Alison J. Friedli[9], Julián Galvez Serna[16,39], Esteban A. Garcia-Migani[40], Anja Genade[36,41], Kai Getrost[22], Ricardo A. Gil-Hutton[40], German N. Gimeno[42], Eli Joseph Golub[5], Giovanni Francisco González Murillo[26], Michael D. Grusin[43], Sebastian Gurovich[35], William H. Hanna[22], Santiago M. Henn[35], P. C. Hinton[9], Paul J. Hughes[5], John David Josephs Jr[5], Raul Joya[44], Joshua A. Kammer[45], Brian A. Keeney[1], John M. Keller[9], Emily A. Kramer[46], Stephen E. Levine[10,17], Carey M. Lisse[27], Amy J. Lovell[47], Jason A. Mackie[48], Stanislav Makarchuk[49], Luis E. Manzano[50], Salma Sylla Mbaye[19], Modou Mbaye[19], Raul Roberto Melia[51], Freddy Moreno[52], Sean K. Moss[9], Diene Ndaiye[53], Mapathe Ndiaye[54], Matthew J. Nelson[5], Catherine B. Olkin[1], Aart M. Olsen[22], Victor Jonathan Ospina Moreno[55], Jay M. Pasachoff[56], Mariana Belen Pereyra[51], Michael J. Person[17], Giovanni Pinzón[57], Eduardo Alejandro Pulver[51], Edwin A Quintero[50], Jeffrey R. Regester[58], Aaron Caleb Resnick[48], Mauricio Reyes-Ruiz[59], Alex D. Rolfsmeier[9], Trina R. Ruhland[22], Julien Salmon[1], Pablo Santos-Sanz[60], Marcos Ariel Santucho[51], Diana Karina Sepúlveda Niño[26], Amanda A. Sickafoose[11,17,36], José S. Silva[25], Kelsi N. Singer[1], Joy N. Skipper[5,61], Stephen M. Slivan[17,62], Rose J. C. Smith[63], Julio C. Spagnotto[64], Andrew W. Stephens[65], Samuel D. Strabala[9], Francisco J. Tamayo[66], Henry B. Throop[11], Andrés David Torres Cañas[39], Labaly Toure[53,67], Alassane Traore[19], Constantine C. C. Tsang[1], Jake D. Turner[5,68], Santiago Vanegas[57], Roger Venable[22], John C. Wilson[5], Carlos A. Zuluaga[17], and Jorge I. Zuluaga[16]

[1] Southwest Research Institute, 1050 Walnut Street, Suite 300, Boulder, CO 80302, USA; buie@boulder.swri.edu
[2] Géosciences Environnement Toulouse, UMR5563 CNRS, IRD and University of Toulouse, 14 Avenue Edouard Belin, F-31400, Toulouse, France
[3] MESRI Allées Papa Gueye Fall Dakar, Sénégal
[4] ASPA 15, nord Foire Dakar, Sénégal
[5] University of Virginia, Department of Astronomy P.O. Box 400325, Charlottesville, VA 22904, USA
[6] IMCCE, Observatoire de Paris 77 av. Denfert-Rochereau, F-75014, Paris, France
[7] PSL Research University, CNRS, Sorbonne Université UPMC Univ. Paris 6, France
[8] Direction de la Formation et de la Communication DFC/MEN Mermoz pyrotechnie Dakar, Sénégal
[9] University of Colorado—Boulder, 2000 Colorado Avenue, Boulder, CO 80309-0390, USA
[10] Lowell Observatory, 1400 W Mars Hill Road, Flagstaff, AZ 86001, USA
[11] Planetary Science Institute, 1700 East Fort Lowell, Suite 106, Tucson, AZ 85719, USA
[12] Herzberg Astronomy and Astrophysics Research Centre, National Research Council of Canada, 5071 West Saanich Road, Victoria BC V9E 2E7, Canada
[13] NASA HQ, Planetary Science Division, 300 E. Street, SW, Washington DC 20546, USA
[14] CADIC-CONICET, Bernardo Houssay #200, 9410 Ushuaia, Tierra del Fuego, Argentina
[15] Université Côte d'Azur, Observatoire de la Côte d'Azur, UMR7293/CNRS CS F-34229, Nice, France
[16] Universidad de Antioquia, Calle 70 No. 52-21, Medellín, Colombia
[17] Massachusetts Institute of Technology, Department of Earth, Atmospheric and Planetary Sciences, 77 Massachusetts Avenue, Cambridge, MA 02139, USA
[18] IATE-OAC, Universidad Nacional de Córdoba-CONICET, Laprida 854, X5000 BGR, Córdoba, Argentina
[19] Université Cheikh Anta Diop Dakar-Fann, Sénégal
[20] ENSTA Bretagne 2 Rue François Verny, F-29200, Brest, France
[21] Sopra-Steria Infrastructure and Security Services 1 avenue du Général Juin, F-92360, Meudon, France
[22] International Occultation Timing Association (IOTA)[69]
[23] Universidad Nacional de Mar del Plata Dean Funes 3350 Mar del Plata, Argentina
[24] Universidad de Buenos Aires Intendente Güldes 2160—Ciudad Universitaria—Capital Federal—Buenos Aires, Argentina
[25] CONACYT—Instituto de Astronomía, Universidad Nacional Autónoma de México, Km. 107 Carretera Tijuana-Ensenada, Ensenada Baja California, México.C.P. 22860, México
[26] Colegio Abraham Maslow Calle 1C #5-03 Chía, Colombia
[27] Johns Hopkins University, Applied Physics Laboratory 11000 Johns Hopkins Road, Laurel, MD 20723, USA
[28] Association Française d'Astronomie 17, Rue Emile Deutsch de la Meurthe, F-75014 Paris, France
[29] RECON, The Dalles, Oregon, USA
[30] LESIA, Observatoire de Paris, Université PSL, CNRS, Sorbonne Université, Univ. Paris Diderot, Sorbonne Paris Cité 5 place Jules Janssen, F-92195 Meudon, France
[31] Karlsruhe Institute of Technology Institute for Meteorology and Climate Research Atmospheric Environmental Research Division (IMK-IFU) Campus Alpin Kreuzeckbahnstrasse 19 D-82467 Garmish-Partenkirchen, Germany
[32] Institut Sénégalais de Recherches Agricoles Direction Générale : Bel-Air, Route des Hydrocarbures BP : 3120, Dakar, Sénégal
[33] Centre Nationale de Recherches Agronomiques CNRA (ISRA) Bambey BP 53 Bambey, Sénégal
[34] KinetX Aerospace 2050 E. ASU Circle, #107; Tempe, AZ 85284, USA
[35] Universidad Nacional de Córdoba, Córdoba, Argentina

[36] South African Astronomical Observatory, 1 Observatory Road, Observatory, Western Cape, 7925, South Africa
[37] Université Alioune DIOP de Bambey BP 30, Bambey, Sénégal
[38] Mathematics and Physics, Queen's University, Belfast, UK
[39] Observatorio Astronómico Instituto Tecnológico Metropolitano, Calle 54 A #30-01, Medellín, Antioquia, Colombia
[40] Grupo de Ciencias Planetarias, FCEFyN, Universidad Nacional de San Juan and CONICET Av. José I. de la Roza oeste 590, Rivadavia, San Juan, J5402DCS, Argentina
[41] University of Cape Town, Rondebosch, Cape Town, 7700, South Africa
[42] Gemini Observatory c/o AURA, Casilla 603, La Serena, Chile
[43] SparkFun Electronics, 6333 Dry Creek Parkway, Niwot CO 80503, USA
[44] Universidad Sergio Arboleda Calle 74 # 14–14—Bogotá, Colombia
[45] Southwest Research Institute, San Antonio, TX, USA
[46] Jet Propulsion Laboratory, 4800 Oak Grove Drive, Pasadena, CA, 91109, USA
[47] Agnes Scott College, 141 E College Avenue, Decatur, GA 30030, USA
[48] Amherst College, 220 South Pleasant Street, Amherst, MA 01002, USA
[49] National Commission on Space Activities of Argentina (CONAE) Av. Paseo Colon 751, Buenos Aires, Argentina
[50] Astronomical Observatory, Technological University of Pereira, Cr 27 #10-02 Barrio Álamos, Pereira, AA 97, Colombia
[51] Observatorio Astronómico Córdoba Laprida 854— Córdoba, Argentina
[52] Colegio Gimnasio Campestre, Calle 165 No 8 A-50 Bogotá, Colombia
[53] Université Gaston Berger, BP 234, Saint-Louis, Sénégal
[54] University of Thies, UFR Sciences de l'Ingénieur BP 967 A Thiès, Sénégal
[55] Telescopios Medellín, Corporación de Astrofotografía de Medellín y Oriente, Calle 42# 108a—215, Medellín, Colombia
[56] Williams College-Hopkins Observatory, 33 Lab Campus Drive, Williamstown, MA 01267-2565, USA
[57] Observatorio Astronómico Nacional, Universidad Nacional de Colombia, Carrera 45 # 26-85, Bogotá, Colombia
[58] High Point University, 1 University Parkway, High Point NC 27268, USA
[59] Universidad Nacional Autónoma de México, Instituto de Astronomía, Ensenada, MÉxico
[60] Instituto de Astrofísica de Andalucía (CSIC), Glorieta de la Astronomía, s/n, E-18008-Granada, Spain
[61] Green Bank Observatory, 155 Observatory Road, Green Bank, WV 24944, USA
[62] Wellesley College, Department of Astronomy, Wellesley, MA 02481, USA
[63] Software Bisque, 862 Brickyard Cir, Golden, CO 80403, USA
[64] Observatorio El Catalejo Mussio 255, Santa Rosa, La Pampa, Argentina
[65] Gemini Observatory, Hilo, HI 96720, USA
[66] Universidad Autónoma de Nuevo León, Pedro de Alba s/n, San Nicolás de Los Garza, Nuevo León, México
[67] Geomatica Dakar, Sénégal
[68] Cornell University, Department of Astronomy, Ithaca, NY 14853, USA

Abstract

We present the results from four stellar occultations by (486958) Arrokoth, the flyby target of the *New Horizons* extended mission. Three of the four efforts led to positive detections of the body, and all constrained the presence of rings and other debris, finding none. Twenty-five mobile stations were deployed for 2017 June 3 and augmented by fixed telescopes. There were no positive detections from this effort. The event on 2017 July 10 was observed by the Stratospheric Observatory for Infrared Astronomy with one very short chord. Twenty-four deployed stations on 2017 July 17 resulted in five chords that clearly showed a complicated shape consistent with a contact binary with rough dimensions of 20 by 30 km for the overall outline. A visible albedo of 10% was derived from these data. Twenty-two systems were deployed for the fourth event on 2018 August 4 and resulted in two chords. The combination of the occultation data and the flyby results provides a significant refinement of the rotation period, now estimated to be 15.9380 ± 0.0005 hr. The occultation data also provided high-precision astrometric constraints on the position of the object that were crucial for supporting the navigation for the *New Horizons* flyby. This work demonstrates an effective method for obtaining detailed size and shape information and probing for rings and dust on distant Kuiper Belt objects as well as being an important source of positional data that can aid in spacecraft navigation that is particularly useful for small and distant bodies.

Unified Astronomy Thesaurus concepts: Kuiper belt (893); Astrometry (80); Classical Kuiper belt objects (250); Stellar occultation (2135)

Supporting material: data behind figures

1. Introduction

The *New Horizons* extended mission target was (486958) Arrokoth, previously known as 2014 MU$_{69}$ (Stern et al. 2018) and informally as Ultima Thule. This cold classical Kuiper Belt object was discovered in 2014 by a targeted search (Buie et al. 2018; Porter et al. 2018) with the *Hubble Space Telescope* (*HST*). Through the end of 2018, we continued to follow Arrokoth to collect astrometry and photometry with *HST*. The mean apparent magnitude is $R = 27$ mag with an absolute

magnitude of $H_R = 11$ (Buie et al. 2018; Benecchi et al. 2019). It is important to realize Arrokoth is at the limit of capability of *HST* and no ground-based facility has successfully detected Arrokoth. In the case of *HST*, the detection limit is set by the size of the telescope. From the ground, larger telescopes are available but the increase in light-gathering power is lost due to the poorer image quality imposed by the atmosphere combined with the extremely crowded background stellar field. There are very effective techniques for removing the stellar background but these techniques cannot remove the noise introduced by the stars. This noise component effectively dictates the limiting magnitude of the subtracted images. Data with better seeing do

reach fainter limits, but our best ground-based search data missed detecting Arrokoth by about one stellar magnitude.

The *New Horizons* mission team needed as much information about the target as possible prior to the flyby of Arrokoth on 2019 January 1 (UT). The spatial resolution of *HST* is about 1200 km per pixel in our imaging data. Stellar occultations provide higher spatial resolution data, typically at or better than 1 km, that greatly exceed what is possible with *HST*. However, a successful occultation has its own challenges. The target body must pass close enough to a star when it can be seen from somewhere on Earth that has good weather. We also must be able to accurately predict where the shadow will be so that telescopes can be deployed to the correct location to record the event. With an object as small as Arrokoth, the probability of its shadow crossing a fixed observatory is very, very low. Given a suitable opportunity, an occultation can do two important things for a mission. First, we are able to measure the projected area of the body and thus infer its albedo when combined with its absolute magnitude, provided enough suitably placed stations can observe the event. Measuring the albedo was important to *New Horizons* as input to the design of the imaging sequences to know the signal-to-noise ratio (S/N) that a given observation would yield. Second, the occultation data provide astrometry. At the time of the occultation, we have precise knowledge of the position of the body relative to the star. With a sufficiently accurate star position, this information translates to astrometric data that is at least a factor of 100 better than a single *HST* image and subject to completely different potential systematic errors. These astrometric constraints were expected to be very important for improved orbit estimates prior to the encounter for both navigation of *New Horizons* as well as pointing information for the cameras.

The albedo of Arrokoth was clearly one of our measurement objectives, but it also played a role in building a successful observing strategy for the deployment for the occultation observations. Using our absolute magnitude estimate of $H_V = 11.1$, a 4% albedo implies a diameter of 40 km. Ignoring the photometric errors on the absolute magnitude, this represented a practical upper limit to its size. A lower limit on size was harder to pin down, but at 20% albedo, the diameter would have been 20 km. This plausible range in size combined with the uncertainty of the orbit estimation played a strong role in the occultation deployment. The heliocentric distance of Arrokoth in 2017 was 43.3 au. At that distance, the scale on the plane of the sky was 31.4 km mas^{-1}. These spatial scales required knowing the position of the object and the star to at least 1 mas for a reasonable chance at a successful multichord occultation.

The orbit for Arrokoth indicates that it is a cold classical Kuiper Belt object ($a = 44.4$, $e = 0.038$, $i = 2.45$; Porter et al. 2018). Observations of other cold classicals reveal a population with a very high fraction of equal-mass binary objects (Noll et al. 2008; Nesvorný et al. 2010; Fraser et al. 2017). The *HST* observations showed no signs of binarity, but we expected an occultation to probe at a much smaller spatial scale.

We present here a description of results for three stellar occultation observation campaigns in 2017 and one campaign in 2018. All of the campaigns returned useful data to constrain the size, shape, and orbit of the *New Horizons* extended mission target.

2. General Background on Events

Our first step for this project was to search the USNO CCD Astrograph Catalog (Zacharias et al. 2013) for candidate stars for occultations in 2017. This search provided a list of three good candidate stars. The positional uncertainties on these stars were too high to get a useful prediction, but they did support the earliest stages of planning. Based on this initial information, we requested time on NASA/DLR's Stratospheric Observatory for Infrared Astronomy (SOFIA), which the telescope allocation committee approved. However, further analysis indicated that SOFIA could only support one of the three opportunities because of logistical constraints. Also at this time, we applied for time on other large telescope facilities and put the word out to the community about these opportunities.

Other than SOFIA, which is mobile, the large telescope facilities were unlikely to be in the right place for a solid-body event. However, all of them could be useful for probing the Arrokoth Hill sphere for additional material, especially rings or extended dust structures. No such material was found, and those results are described further in Young et al. (2018), which excluded rings with radii up to 1000 km and widths greater than 720 m. The key to success for a solid-body detection was a large number of mobile ground stations.

Based on our estimates of the final prediction uncertainties we built a plan for 25 mobile stations. *New Horizons* procured 22 systems for this project that are based at Southwest Research Institute (SwRI) in Boulder, Colorado. These identical systems were each assigned a system code between T01 and T22. In addition, the University of Virginia (UVA) provided three additional systems, all of differing designs. We assigned these systems codes T23 to T25, and we will describe these separately.

We relied heavily on astrometric support catalogs for this project. During the project, we used many different catalogs. However, getting a good prediction required using the same catalog to calibrate the *HST* astrometry and obtain the position of the occultation star. In the earliest phase of this project, we used a special catalog developed by S. Gwyn at the Canadian Astronomy Data Centre using data from the Canada–France–Hawaii Telescope Megacam system. This catalog had better internal consistency than any other catalog available at the time; however, this catalog did not have useful proper motion information. To overcome this limitation, we used mean apex proper motion corrections (Gwyn 2014). This mean correction was acceptable for the orbit estimation but was inadequate for the positions of the occultation stars themselves.

The release of the *Gaia* Data Release 1 (DR1) catalog (Gaia Collaboration et al. 2016) allowed us to revise and improve the support catalog and positions of the occultation stars. Essentially all of the stars we used from the catalog were too faint to have proper motions from DR1, so we were again forced to use mean proper motions. We made an additional effort to search for other epochs of data on these fields to constrain the proper motions of the occultation stars. We found data in the MAssive Compact Halo Object (MACHO) archives (Allsman et al. 2001), which provided a slightly improved set of predictions; however, those predictions were still inadequate.

We obtained *HST* images of all candidate occultation stars. The *HST* images showed no signs of stellar duplicity. The images captured the positions of the stars near the epoch of the occultation so that the projected uncertainty from proper

Table 1
Occultation Star Data

Star	Epoch (year)	R.A.(α) (deg)	σ_α (mas)	Decl.(δ) (deg)	σ_δ (mas)	Parallax (mas)	PM$_\alpha$ (mas yr^{-1})	PM$_\delta$ (mas yr^{-1})	G (mag)
MU20170603	2015.5	285.8937182917	0.040	−20.5775960556	0.039	0.326 ± 0.053	−0.504 ± 0.078	0.567 ± 0.071	15.27
	2017.419	285.8937182238	0.158	−20.5775957188	0.142	⋯	⋯	⋯	⋯
MU20170710	2015.5	285.1734150250	0.040	−20.6457042778	0.038	0.493 ± 0.042	2.988 ± 0.081	−0.922 ± 0.075	15.53
	2017.520	285.1734168060	0.169	−20.6457047916	0.156	⋯	⋯	⋯	⋯
MU20170717	2015.5	285.0345477417	0.048	−20.6605479583	0.047	0.506 ± 0.056	0.451 ± 0.090	−4.696 ± 0.078	12.75
	2017.539	285.0345479854	0.190	−20.6605506170	0.166	⋯	⋯	⋯	⋯
MU20180804	2015.5	286.0894861917	0.023	−20.5934747944	0.022	2.486 ± 0.026	8.669 ± 0.046	−12.310 ± 0.043	13.381
	2018.589	286.0894938000	0.144	−20.5934853695	0.135	⋯	⋯	⋯	⋯

Note. Positions are all referenced to EME2000.

motion would not dominate the prediction uncertainty. As we were working to extract this information, the *Gaia* Mission graciously agreed to provide prerelease positions from the *Gaia* Data Release 2 (DR2) catalog which had just finished its initial processing. With DR2 in hand, there was no need to get positions from the *HST* data.

The *Gaia* DR2 prerelease subcatalog covered an area of the sky encompassing all of the *HST* observations of Arrokoth from the discovery epoch in 2014 through the end of 2017. The area also included the occultation stars. This catalog contained proper motions and uncertainties for all listed stars. The catalog density in these areas was high enough that the final uncertainty of the WCS calibration for the *HST* images was a negligible component of the occultation predictions. Having *Gaia* DR2 information on the occultation stars was fundamentally important because it meant all of the astrometry for Arrokoth and all of the occultation stars were in the same catalog system. More significantly, DR2 was referenced to the same Inertial Coordinate Reference Frame (ICRF) used for navigation of *New Horizons*. This allowed us to quantify the uncertainties for the *HST* observations, the orbit estimation, and the occultation predictions themselves, and ultimately provide useful positional data that would aid with navigation for the *New Horizons* flyby. Table 1 provides the final positions of the stars used in support of the occultation campaigns. The first line for each star provides the full DR2 catalog entry (epoch = 2015.5). The second line contains the positions at the epoch of the event as well as the propagated uncertainties. For the catalog positions, we tabulate the parallax, proper motions in R.A. (PM$_\alpha$) and decl. (PM$_\delta$), and the *Gaia* "G" magnitude. More information can be found about the *Gaia* catalog values in Gaia Collaboration et al. (2018). Although the uncertainties of all stars were much better than any prior occultation event work, these low uncertainties at the epoch of the events were still important. We will return to this point later in Section 7.7. In particular, the star from 2018 is clearly much closer than the rest as seen by its higher parallax and proper motion. Without the *Gaia* results, this last star would have been completely impossible given the tight targeting requirements for these occultation attempts.

Another important component of event predictions is the orbit estimation for Arrokoth. We had an ongoing program with *HST* to observe the object periodically and collect additional astrometry, starting in 2014 with its discovery and continuing through 2018 October. Our baseline observing cadence was five epochs of data per year, spread out over the

apparition. Each epoch consisted of five 370 s exposures, usually within a single visibility window from *HST* (one orbit). In 2017, a special lightcurve campaign added an additional 24 orbits of astrometric data just prior to the SOFIA occultation attempt (Benecchi et al. 2019).

3. Mobile Instrumentation

3.1. 2017 Summary

3.1.1. SwRI–NH Systems, T01–T22

We assembled the 22 mobile T01–T22 systems with commercially available components plus custom storage and shipping crates. Each system included a Skywatcher 16 inch (40 cm) Dobsonian telescope with computerized drive electronics. Each telescope provided an $f/4.4$ beam at the Newtonian focus. Each telescope's secondary housing is in a short tube held up from the primary support tube by three rods. The secondary housing collapses down next to the primary tube for storage and transportation. The alt-az drive system design allowed us to move the telescope either manually or with the motors without loss of pointing. Once properly aligned, the telescope automatically tracks a point on the sky but the field rotates slowly on the detector as it tracks. Because these telescope systems did not have GPS installed, each system required manual entry of time and position at the start of each observing session. The optics were reasonably robust but did require some attention and recollimation with each use. The primary mirror support rarely needed realignment but we found that the secondary inevitably moved during transport. A laser collimator became an essential component of each field support kit. We also learned that these telescopes are susceptible to stray light interfering with the camera. In addition, relatively light winds can shake the telescope: image motion becomes apparent at 5 mph (8 kph); we found it very difficult to use the telescope at all over 10 mph (16 kph) without a mitigation strategy.

We chose a QHY174M-GPS camera, using a thermoelectrically cooled CMOS detector with a built-in GPS receiver. The camera's array size is 1920 × 1200 pixels and provides a field of view of 21′ × 13′ with a pixel size of 0″.67. We used SharpCap[70] to read out the detector and save the data. This software can write each image to a separate FITS file while also recording the GPS-based start time for each exposure. The

---

[70] https://www.sharpcap.co.uk

software writes the latitude and longitude to the header of each file. Because the camera does not pass out the altitude, we had to manually record the altitude information. All of our systems used SharpCap version 3.0.3938.0 for the entirety of the 2017 campaigns. The GPS position in this version of the software was not always accurate, so we instructed all teams to use another means (usually a cell phone) to record their location. The camera has a fast 12-bit A/D converter but SharpCap shifts the data to the most significant bits of a 16-bit integer. This version of SharpCap allowed a variable system gain setting between 1 and 48: the higher the gain number, the fewer photons per count. As the gain setting is increased, the read noise of the detector decreases while also reducing the dynamic range. The highest effective gain setting was 30, above which the only meaningful change is to further reduce the dynamic range. An approximate gain was 0.004 electrons/DN at GAIN = 30. The read noise was around two to three electrons. We used a temperature set point of 0°C. With this setting, the dark current is negligible.

We verified the timing information of the system by analysis using the Southern EXposure Timing Array (SEXTA) system (Barry et al. 2015). As long as there is a valid GPS fix and an up-to-date leap-second almanac, we found the QHY camera always had the correct start time within the 2 ms precision of the SEXTA. However, the camera captures very little supporting information with the data, and in particular it does not always capture the state of the GPS and almanac download information. Updated firmware was eventually provided but too late to be used for these occultation campaigns. These cameras also do not appear to save the almanac information between uses; therefore, we ran the cameras for at least 20 minutes so that we were certain to get the correct leap-second information. Before the update, the system time was off by 2 s. There were no direct indications that this update happened without watching the clock very carefully. The observing protocol for these systems naturally led to a period of operation before data collection well in excess of the almanac update interval.

We collected data with an inexpensive laptop with a spinning hard disk. This system was not quite capable of 5 Hz readout speeds for full frames, but laptops with solid-state hard drives showed much higher readout speeds, closer to 12 Hz. To enable a faster readout speed, we reduced the number of rows read and saved. This also reduced the field of view. Changing the number of columns made little difference to the speed.

We ran the laptop from its built-in battery in the field. We powered the telescope and camera cooler from a rechargeable sealed lead-acid battery pack. Our observing sessions were rarely longer than 4 hr and the battery capacities were more than adequate for this usage.

We had some variability in overall system performance including a few failures in the field. During the initial transport, the T22 system mirror detached from its steel support structure. We used this system as a source of spare parts during the rest of the 2017 deployment. A few of the telescope systems had significant amounts of backlash in the gears. With care and the calibrations and adjustments noted above, these systems worked sufficiently well for our needs.

3.1.2. UVA Systems, T23–T25

The UVA supplemented the 22 SwRI systems with three additional telescopes: a 24 inch Dobsonian $f/4.2$ telescope

from Hubble Optics (T23), a 14 inch Meade LX200-GPS fork-mounted telescope (T24), and a 14 inch Celestron EdgeHD telescope mounted on a CGE-Pro equatorial mount (T25). The two 14 inch telescopes employed the same QHY174M-GPS sCMOS camera described previously while the 24 inch telescope used a higher performance PCO Gold 4.2 sCMOS camera.

T23: The 24 inch Hubble Optics telescope had more than twice the collecting area of the next largest telescopes in the network. A PCO Gold 4.2 2048×2048 sCMOS camera further augmented the sensitivity of this larger aperture by providing $<1\,e^-$ read noise exposures at high frame rate. The 6.5 μm pixels of the PCO camera provided a pixel scale of $0\rlap{.}''6$ pixel^{-1} and a field of view of $20.5 \times 20\rlap{.}'5$. Binning of the PCO images produced 1024×1024 frames with $1\rlap{.}''2$ pixels.

T24: An $f/6.3$ Meade focal reducer provided a pixel scale of $0\rlap{.}''55$ pixel^{-1} for a QHY camera at the focal plane of the 14 inch Meade telescope. The resulting field of view was $17.6 \times 11'$.

T25: A Starizona Hyperstar on the 14 inch Celestron EdgeHD telescope provided an $f/1\rlap{.}'9$ focus that delivered a pixel scale of $1.77''$ pixel^{-1} on the QHY array. The full field of view of the QHY camera in this configuration was $57 \times 35'$.

3.2. 2018 Summary

All of the systems once again used the QHY cameras with embedded GPS receivers. SharpCap was again used for data collection after upgrading to version 3.1.5219.0. With this version, the error in recording the position was fixed. Most operations were the same as before but the gain control values were a factor of 10 higher in the new software. Thus, our previous "standard" gain value of 30 was now 300. Additionally, the GPS receiver status was now visible all the time on the main control screen to help monitor its state more closely.

3.2.1. SwRI–NH Systems, T01–T22

We used the same systems for both the 2017 and 2018 events after minor repairs such as replacing the mirror for T22. We shipped the T01–T19 systems by ocean freight to Sénégal and the T20–T22 systems via air freight to Bogotá, Colombia. Two telescopes failed in the field because they were unable to point and track under computer control. However, we still used these systems by manually pointing the telescope to the proper altitude and azimuth so that we had the occultation star in the field of view at the time of the occultation.

3.2.2. UVA Systems, T23–24

UVA's systems for this deployment consisted of two identical Celestron EdgeHD 14 inch telescopes on CGX-L equatorial mounts. The optical properties of these systems, which included Starizona Hyperstar prime-focus adapters, were identical to the Celestron 14 inch system (T25) used in the 2017 events. This once again provided a scale of $1\rlap{.}''77$ pixel^{-1} on the 5.86 μm pixels of the QHY174M-GPS sensor. Note that the system IDs for the UVA equipment from 2018 do not match the system IDs from 2017.
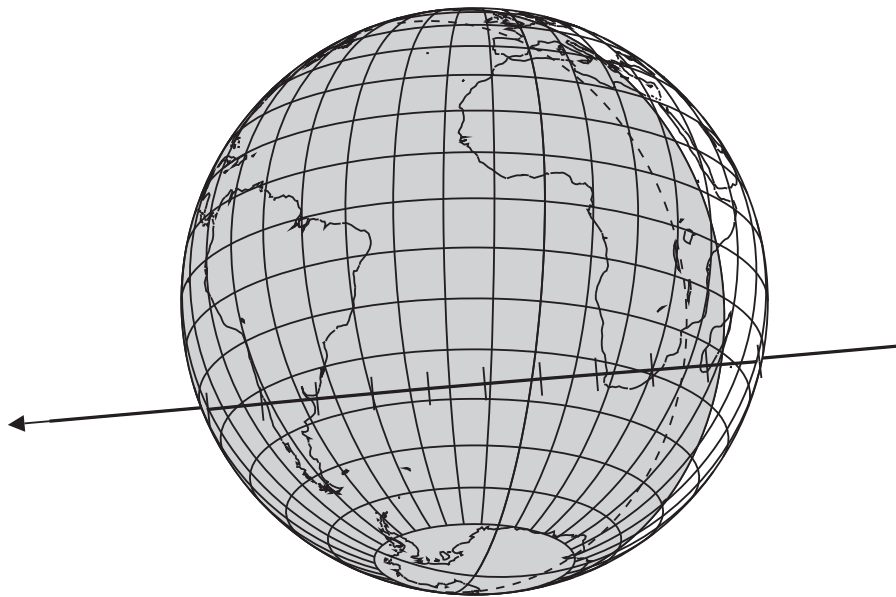
Figure 1. Global view of 2017 June 3 occultation prediction. The figure shows Earth as seen from Arrokoth at the time of geocentric closest approach. The Sun is below the horizon in the regions shaded gray. The dashed line indicates $-12°$ Sun altitude. The solid line indicates the predicted ground track with the width drawn to scale for a 30 km diameter object. The arrowhead indicates the direction of motion, and the ticks are spaced at one minute intervals from 03:07 to 03:17 UT. Shadow velocity was 20.0 km s^{-1}. A 66% illuminated Moon was 103° away from the target at the time of the event but was below the horizon in Africa.

4. 2017 June 3 Event

This event was the hardest because it was both the first attempt with the new field systems and because we had relatively poor orbit constraints on Arrokoth. The initial rough prediction indicated that we could observe the event from both South America and southern Africa. The predicted location shifted significantly in the months leading up to the event. However, from the beginning, our overall plan involved splitting our resources between the two continents to improve our chances of getting useful data. Figure 1 shows the global view of the final prediction. We limited the deployment to ground stations because the expected uncertainty was too high for consideration for a SOFIA flight.

4.1. Prediction

The prediction for this event was finalized very close to deployment. We should have had new astrometry from *HST* in 2017 March, but those observations were lost to an *HST* schedule interruption due to an unrelated technical anomaly. The earliest we were able to reschedule *HST* was 2017 May 1. Until we obtained the 2017 May 1 data, the most recent observation data were from 2016 October 24. The new data provided a substantial increase in the total arc length of the Arrokoth astrometry, from 2.3 yr to 2.9 yr with a corresponding decrease in the extrapolation to the time of the event from seven months down to just one month. Also on May 1, we obtained the *HST* observations of the three 2017 target stars. We used these target star observations for astrometry and to search for stellar duplicity. We did not find any stellar companions or duplicity in the *HST* images down to the resolution limit of the data (∼40 mas).

We were able to significantly improve the orbit estimate with this new astrometry; however, we still needed to resolve fundamental questions about the position of the occultation star and the associated uncertainty. We began working on the *HST*

data to improve our constraints on the star positions. However, on 2017 May 6, we were provided access to preliminary data from the planned *Gaia* DR2 (Gaia Collaboration et al. 2016). Those data included the occultation stars among the stars in the region around Arrokoth back to 2014. We reprocessed all of the *HST* data with updated reference stars to improve the orbit estimate. Within a week, we had refined the event prediction enough so that we could determine where to deploy the observing teams and begin the process of shipping equipment and setting up travel logistics. We obtained one more epoch of data from *HST* on 2017 May 25, just a day before the first teams left. We completed the final prediction a couple of days before the June 3 event with a cross-track uncertainty of 44 km. The in-track (timing) error was 67 km (3.3 s). Unless otherwise stated, all uncertainties stated in this work are 1σ values.

4.2. Deployment

We had 24 mobile stations available for deployment. The equipment was all sent via air freight to Argentina and South Africa due to the extremely tight schedule. Local movement of the systems was handled by individual vehicles carrying one team and system.

Even with this large number of stations, we could not cover all possible cases for the object, e.g., small versus big given the prediction uncertainty. To guide the deployment process, we used a Monte Carlo simulation. The simulation uses the cross-track positions for the observing locations relative to the prediction. The model employs a circular representation of the occulting body with an adjustable diameter. For a given size and set of observing locations, we draw a random location for the center line from a normal distribution consistent with the prediction and its uncertainty. For a given draw, we compute the chord length for each site (or note a miss) and record the number of chords seen. To be counted, we required a chord to be no shorter than half the diameter. This adjustment recognized that we might not see very short grazing chords

ID	Team	Latitude (deg)	E Longitude (deg)	Elevation (m)	FWHM (pixels)	Sky (counts)	Comments
T01	M. Buie, A. Ocampo, S. Makarchuk	−33.046832	−68.325955	627	7.4	5411	poor tracking at midtime
T02	J. M. Pasachoff, M. Lu, J. Jewell, S. Gurovich	−33.609167	−69.006944	882	7.3	6460	
T03	C. Olkin, R. Reaves	−33.946734	−67.981331	604	8.6	4041	flares from traffic
T04	W. Hanna, C. Erickson, A. Soto	−33.053972	−68.778343	826	7.9	12097	
T05	A. Parker, K. Getrost	−33.649326	−68.058762	582	9.6	4214	
T06	J. Dunham, P. Tamblyn	−33.218226	−68.612913	720	9.4	6999	
T07	D. Dunham, A. Olsen	−34.011530	−69.089410	1215	10.2	5033	
T08	S. Slivan, R. Venable	−32.747256	−68.479500	598	6.2	6038	
T09	D. Duncan, A. Friedli	−32.851725	−68.392300	640	6.9	8026	flares from traffic
T10	S. Conard, B. Keeney, J. Rabassa	−33.309463	−68.900784	938	7.1	5375	
T11	L. Wasserman, S. Moss, M. Camino	−32.564267	−68.672067	600	8.0	4549	
T12	S. Levine, C. Zuluaga	−34.100796	−67.942469	559	6.8	5612	
T13	S. Porter, C. Danforth	−32.001628	+18.777307	91	6.2	3054	some clouds
T14	A. Zangari, C. Carter	−31.524233	+23.589731	1346	6.1	3108	
T15	C. Tsang, R. Smith	−31.501944	+18.912778	246	6.1	3821	
T16	E. Young, A. Rolfsmeier	−32.352265	+18.937847	146	5.1	1707	
T17	J. Regester, E. Kramer	−32.121767	+19.054971	496	4.1	1372	
T18	M. Person, A. Arredondo	−31.780278	+18.622902	35	6.0	2816	
T19	J. Moore, S. Strabala	−31.286389	+23.699167	1287	6.4	2898	
T20	T. Blank, P. Maley, H. Throop, N. Erasmus	−31.046868	+22.992324	1272	4.1	1780	
T21	A. Verbiscer, A. Caspi, T. Ruhland	−32.564777	+18.977851	203	6.0	3222	clouds at the end
T23	M. Nelson, P. Hughes	−30.713013	+23.904314	1241	2.1	⋯	
T24	B. Andersen, J. Wilson	−30.618650	+22.897806	1187	5.9	16	
T25	M. Skrutskie, D. Josephs	−30.670305	+23.567372	1193	1.8	2380	

Note. Positions are all referenced to WGS84 datum.

given the anticipated noise in the data. The tool also provides additional provision for a small random component to the site location. We could always indicate a desired location to a team, but local constraints could force them to set up some distance away from the desired location. By using this extra random component, we were able to give guidance on how close each team needed to be to their assigned location. For this event, the teams needed to observe from within a 1 km region centered on the assigned location. After running 10,000 trials, we then generate a histogram as a function of the number of chords from which to evaluate a given scenario.

A baseline goal for this event was to observe or rule out the largest size based on a 4% albedo. The deployment strategy was guided by the desire to obtain a strong constraint using just one set of stations (either T01–T12 or T13–T25, but not both). A spacing of 15.5 km between sites was chosen so that we would have no more than a 3% chance of a null result (zero chords). This spacing covered a range of $\pm 1.9\sigma$ or ± 83 km and had a 93% chance of getting two or more chords. Given the 44 km cross-track uncertainty for this event, it would have taken a much larger number of mobile stations to address a smaller object scenario, and we had to accept a poorer constraint for that case. With a half-space shift between Argentina and South Africa, the net spacing if all sites participated in the optimum plan would have been 7.8 km. The same pattern would have had a 5% chance of a null result but an 84% chance of a single-chord outcome on a 20 km object. This tool was very effective in guiding the Mendoza, Argentina, area deployment where the teams had a great deal of flexibility without the need for detailed site selection scouting days before the event. We made adjustments up to the last hours before teams left for their sites. The teams in South

Africa required more advance warning, due to more complex logistics for site access. We were able to use this same tool to assess the outcome for the actual site locations after the event.

4.3. Observations

Twelve stations in each continent successfully deployed and all collected useful data. Table 2 provides a summary of the mobile stations. All Earth-based positions for this deployment are provided on the WGS84 datum. Every station in Argentina had clear conditions but some had to deal with preventing the formation of dew on the telescope optics. The teams near Clanwilliam, South Africa, had variable amounts of clouds, but the teams that headed east had clear skies. Because the Moon had set in South Africa, the teams in South Africa experienced systematically lower background levels. They also had better seeing than the teams in Argentina. The Argentina teams observed with a 66% illuminated Moon and higher contributions from light pollution, which resulted in generally higher background noise levels. The background information for T23 is not provided, due to it being a very different system and the intercomparison with other stations is not particularly useful. All stations used a 0.5 s exposure time. The shadow speed of $20 \, \text{km s}^{-1}$ meant a central chord on a $D = 40$ km body would be four frames. We ran all observations for 45 minutes centered on the local predicted event midtime. We designed this range of time to cover the stable region of the estimated Hill sphere for Arrokoth. We did not see any lightcurve signatures related to Arrokoth in any of the data sets—fixed or mobile. Figures 2 and 3 show the data from the mobile stations. These figures only show data within 30 s of the predicted event midtime. The lightcurves are sorted north to south across the predicted track.
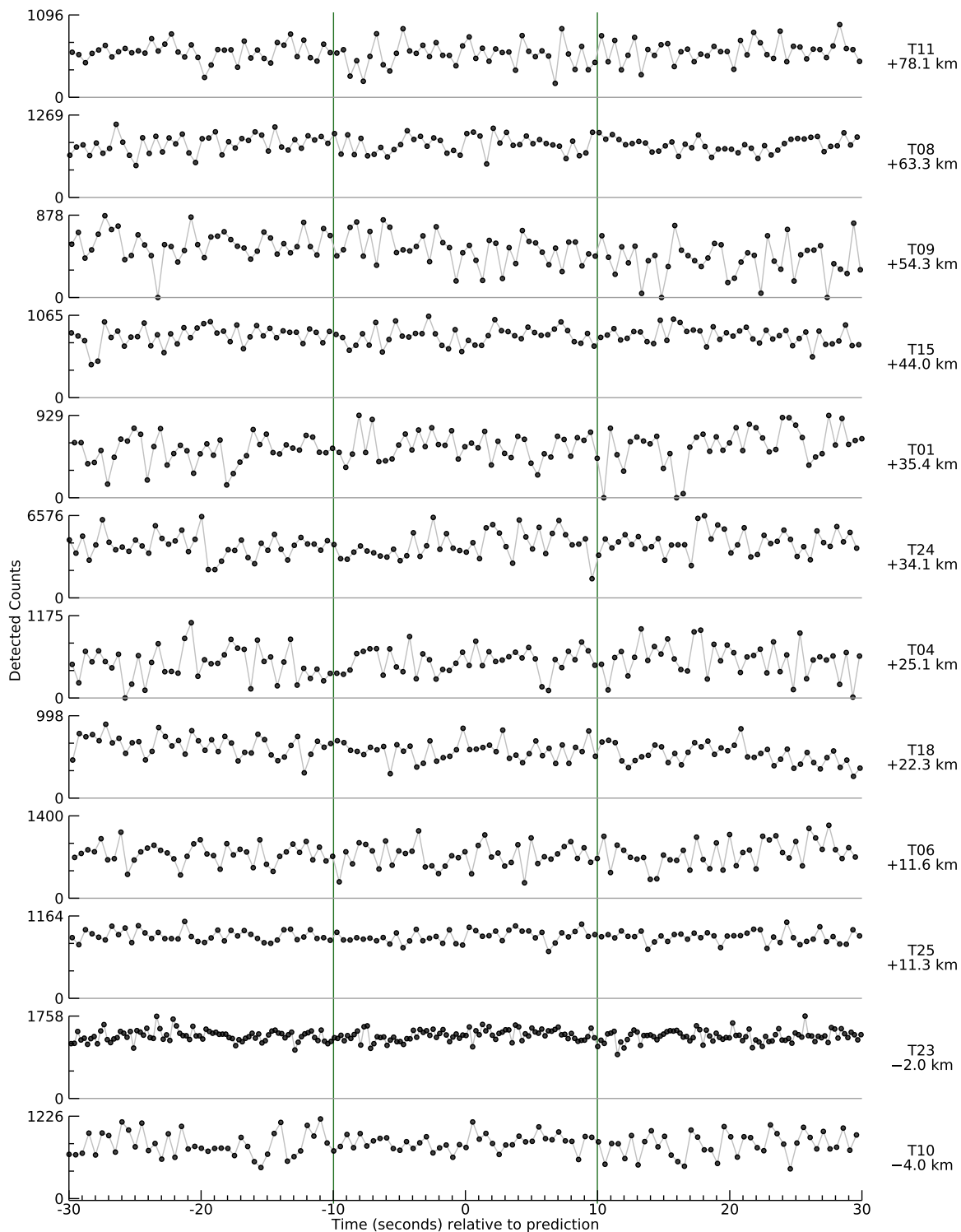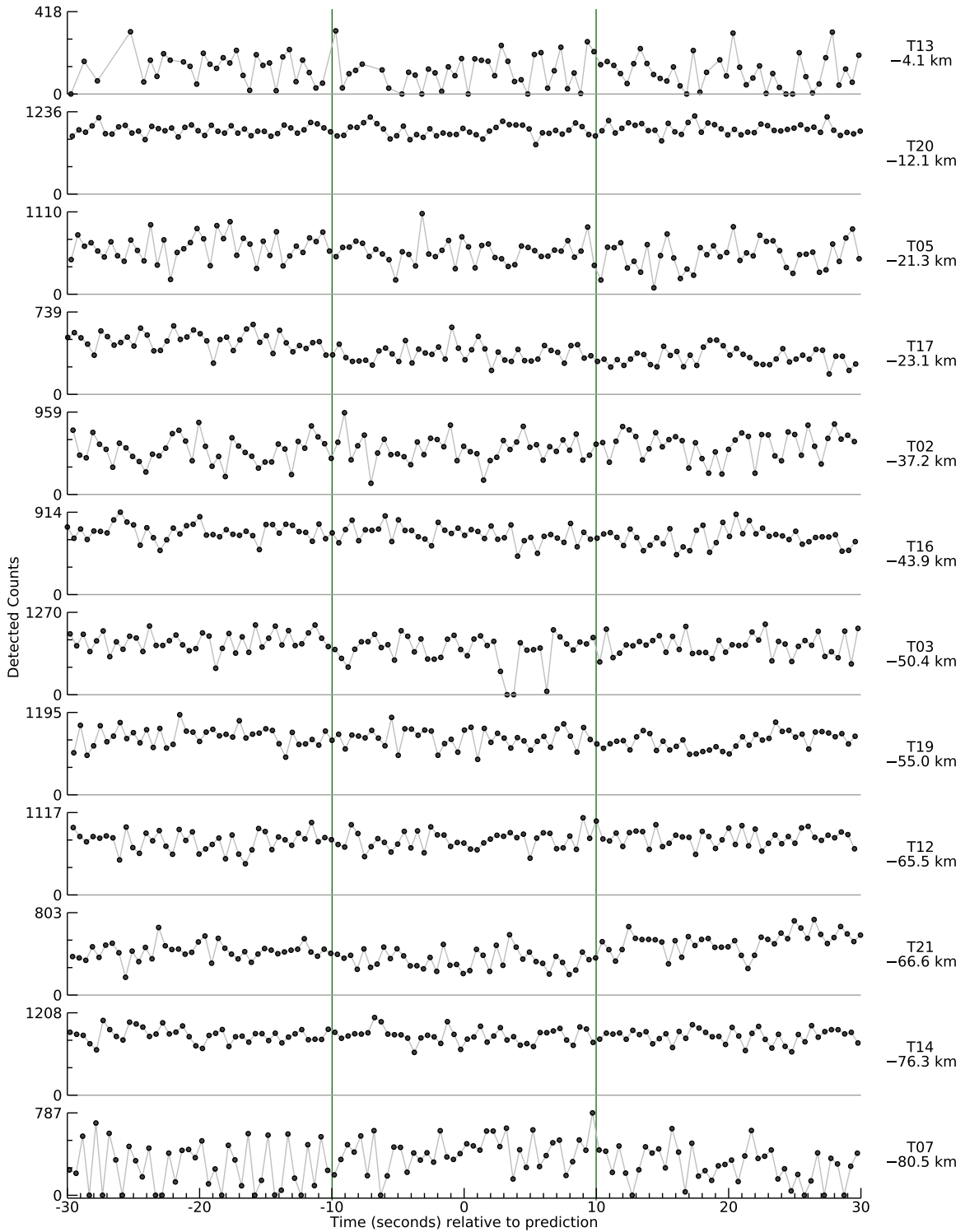
Figure 2. Observations from the 2017 June 3 occultation, part 1. The figure shows the lightcurves from the northern half of the data collected by the mobile stations. Each subplot is labeled on the right with the team number and the cross-track offset. The team numbers are cross-referenced with Table 2. The plots indicate the signal level from each station—higher numbers indicate higher signal levels. The green vertical lines indicate the predicted 3σ uncertainty limits for the event.

(The data used to create this figure are available.)

There is a lot of variability in data quality as can be seen in the plots. Most of the apparent dropouts in these data are due to high winds and severe image smearing. In these cases, we visually examined the data to confirm that the target star was, in fact, still visible and the dropout was not an occultation.

4.4. Fixed Stations

The mobile station effort was augmented by fixed-station observations. Those stations participating are listed in Table 3. Key data sets from these are summarized in the remainder of this section.

Figure 3. Observations from the 2017 June 3 occultation, part 2. The figure shows the lightcurves from the southern half of the data collected by the mobile stations. Each subplot is labeled on the right with the team number and the cross-track offset. The team numbers are cross-referenced with Table 2. The plots indicate the signal level from each station—higher numbers indicate higher signal levels. The green vertical lines indicate the predicted 3σ uncertainty limits for the event.

(The data used to create this figure are available.)

4.4.1. Gemini

We acquired observation data at the Gemini-south telescope on Cerro Pachón using the Gemini Acquisition camera (AC) and a similar methodology to Fraser et al. (2013). The AC is a shutterless $1\,k \times 1\,k$ frame-transfer CCD camera with pixel scale of $0\rlap{.}''12\,\mathrm{pixel}^{-1}$ that supports subframe windowing. We acquired a nearly 60 minute sequence centered on the nominal overhead passage time. We positioned the CCD so that the target star and a nearby reference star were fully included in the window. The CCD was read out with 2×2 on-chip binning

Table 3
Fixed Observing Stations

Name	Event	Team	Latitude (deg)	E Longitude (deg)	Elevation (m)	X-track (km)	Comments
Gemini	MU20170603	W. Fraser	−30.240750	−70.736693	2722	384	
SAAO	MU20170603	A. Sickafoose, A. Genade	−32.378944	+20.811667	1760	17	
EABA	MU20170603	M. Santucho, E. Pulver, H. A. Durantini Luca, R. Artola	−31.568442	−64.549836	1350		
Córdoba	MU20170603	C. Colazo, R. Melia	−31.599167	−64.548333	1350		
SARA-CT	MU20170603	A. Bosh	−30.17200833	−70.79916667	2012		observing through clouds
Gemini	MU20170710	W. Fraser	−30.240750	−70.736693	2722		
SOAR	MU20170710	A. Zangari, L. Young, J. Carmargo	−30.237892	−70.733611	2748		
IRTF	MU20170710	S. Benecchi	+19.8262	−155.4719	4205		
SOAR	MU20170717	L. Young, J. Carmargo	−30.237892	−70.733611	2748		
El Leoncito	MU20170717	E. García-Migani, R. Gil-Hutton	−31.798600	−69.295600	2483		very bad seeing
duPont	MU20170717	A. Bosh	−29.01583333	−70.69194444	2380		good weather

Note. EABA = Estación Astrofísica Bosque Alegre, Córdoba

with a window of 88 × 65 binned pixels. We used an exposure time of 0.1 s.

Nominally, the Gemini header creation system creates image timestamps. However, this system was never intended to operate at the high cadences of our sequence. Because of this limitation, we disabled the header creation system to maximize cadence and minimize interexposure deadtime. We created image timestamps by monitoring file creation times that were produced by GPS time within the Linux system. This imaging configuration resulted in a 0.107 s median deadtime due to image readout and file writing. The resulting image cadence was 4.8 Hz.

We debiased and flattened science frames in the usual manner using sky flats. We extracted photometry using the SExtractor software package and calibrated the relative flux of the target star using the brighter reference star. The resulting photometry had a mean S/N of 48. No occulting structures, dust, rings, or solid bodies were seen. The cross-track offset for these data was 384 km, too far away to be relevant for the solid-body occultation.

4.4.2. South African Astronomical Observatory (SAAO)

We also took observations on the 74 inch telescope at the SAAO using one of the Sutherland High-speed Optical Cameras (Coppejans et al. 2011). This instrument is optimized for stellar occultation observations utilizing a frame-transfer CCD which can trigger each image from a GPS. The conditions on the night of the event were good, with scattered, light clouds and seeing of roughly 1″.4. For these observations, we took 27,000 frames starting at 02:47:00.0 UT with a cadence of 0.1 s and a 6.7 ms deadtime. We set the instrument to −70 °C in 3 MHz conventional mode with the 5.2× amplifier, binned 8 × 8 (for a plate scale of 0″.608 pixel^{-1}), and no filter.

We reduced the data using biases taken on the night of the event and flat fields taken the previous night, which was cloudless. We performed photometry on the target star and the one nearby brighter comparison. We carefully selected a background region to avoid other stars in the field. The optimal aperture was 6 binned pixels or 3″.65. Figure 4 shows the resulting differential lightcurve, normalized to one, with an S/N (mean over standard deviation) of 21. These data are the

Figure 4. SAAO observations for the 2017 June 3 occultation. The figure shows the lightcurve obtained from SAAO. We see no event in the data. The solid green lines indicate ±3σ relative to the "may25a" prediction. The dashed purple lines indicate ±3σ relative to the final "ey7" postdiction. The cross-track offset based on "ey7" is 17.4 ± 4.0 km. See Section 7.7 for an explanation of the terms "may25a" and "ey7."

(The data used to create this figure are available.)

closest to the shadow center line and have significantly higher S/N and time resolution compared to the mobile stations. We saw no evidence for any solid-body event. The data have a cadence of roughly 2 km per sample and grazing events as short as 200 m can be ruled out. In the subsequent analysis, we simply treat this as a nondetection and do not consider potential grazing chord constraints. We will return to the constraints provided by these data when discussing the data from all occultation events together (see Section 7.7).

4.5. Results

Based on the final prediction prior to the June 3 event and the actual site locations, the chance of getting zero chords for D = 40 km was 3%. For a D = 40 km object, a single chord
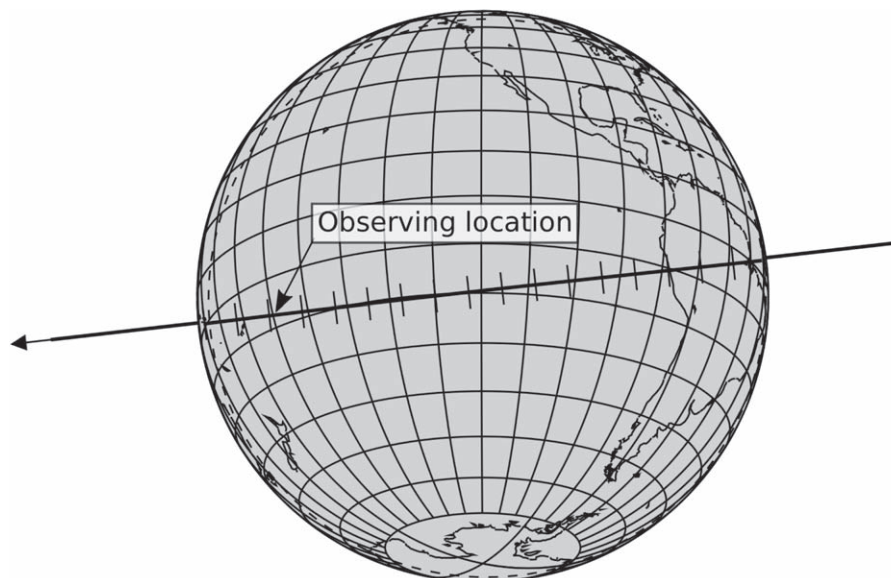
Figure 5. Global view of the 2017 July 10 occultation prediction. The figure shows Earth as seen from Arrokoth at the time of geocentric closest approach. The Sun is below the horizon in the regions shaded gray (the entire globe). The dashed line shows where the Sun is at $-12°$ altitude. The solid line indicates the predicted ground track with the width drawn to scale for a 30 km diameter object. The arrowhead indicates the direction of motion, and the ticks are spaced at 30 s intervals from 07:41:30 to 07:50:00 UT. Shadow velocity was 25.0 km s^{-1}. A 99% illuminated Moon was 17° away from the target at the time of the event.

would be based on multiple frames with the star occulted and could be recognized with high confidence. For $D = 20$ km, the chance of a null result was only 14%. In this case, either zero or one chord would likely be a null result because the chord would be so short. It was very unlikely that we would have seen even smaller objects because the chance of getting a single chord at all was so small. Even if we got a chord, there was a large chance it would be too short to be recognizable. We also did not observe a solid-body event from any fixed site; however, most fixed sites were too far away from the mobile chords to provide much constraint.

Under the assumption that all of our error sources (random and systematic) are known and well characterized, these results indicated that the large and dark case for Arrokoth was unlikely. We chose to then optimize for the small object case for subsequent occultations.

4.6. Limits on Moons and Opaque Rings from Gemini

The nondetection of any occultation in the Gemini data provided upper limits on the presence of dust particles within the Gemini beam. The interexposure deadtime was the limiting factor in the size of detectable particles in the Arrokoth environment. The minimum detectable size was a particle perfectly centered on the occulted star, which would have cast a shadow on the detector that would be mostly contained in the deadtime, but with just enough on-exposure shadow to cause a detectable dip in flux. We consider a 5σ dip such that we would not have expected any one of the ~16,000 exposures to vary by this amount by chance. Thus, in this limiting case, a shadow of duration $t = \frac{5}{\text{S/N}} t_e + t_d$, where $t_e = 0.1$ s was the exposure time and $t_d = 0.107$ s was the deadtime, could have produced a detectable dip in flux. With a ground-track shadow velocity of 20 km s^{-1}, the minimum detectable particle size (or narrow and opaque ring) was 2.3 km.

5. 2017 July 10 Event

We originally considered this event for a large mobile deployment. Because of a number of logistical difficulties, we focused on large aperture observations to search for or constrain the presence of rings or diffuse dust structures. The global view of the ground track in Figure 5 shows some of the difficulties. The shadow only crossed land in regions of South America that were unlikely to be clear. More importantly, this event occurred just 17° from a 99% illuminated moon and the occulted star was the faintest star of the four. The largest effort went into supporting an observation with SOFIA (Temi et al. 2014). Data were collected at other fixed sites but in the end were less constraining than the Gemini data from 2017 June 3.

5.1. Prediction

SOFIA approved this flight opportunity because the likelihood of a positive outcome was deemed sufficient. Of the three 2017 events, it was the only one with a track accessible using a single flight from the summer deployment base of Christchurch, NZ. The primary goal of the flight was to probe the system for material potentially hazardous to *New Horizons*. A secondary goal was to observe a solid-body event; however, it was very challenging to target the aircraft on the occultation track. The support requirements for the SOFIA flight set the timing of the prediction work for this event.

A large observing campaign with *HST* on Arrokoth, timed to be completed just prior to the SOFIA flight, significantly improved the prediction. HST GO-14627 (PI: Benecchi) provided 24 orbits that returned 119 images and resulted in 118 new astrometric measurements during the interval from 2017 June 25 to 2017 July 4 (Benecchi et al. 2019). The goals of the lightcurve investigation dictated the time span and spacing of the observations, while we set the end time of those observations to allow all of these data to be included in the SOFIA prediction, with the smallest temporal gap between the end of data and the time of the occultation opportunity. The

new data set doubled the number of astrometric measurements between this and the previous occultation. We once again reduced all images against the prerelease version of the *Gaia* DR2 catalog (Gaia Collaboration et al. 2018). The vastly improved prediction uncertainty for the cross-track position was 14 km. The in-track error (timing) was 21 km (0.86 s).

5.2. Deployment

Assuming no error in delivering SOFIA to the target point, the odds of getting one chord on a $D = 40$ km object were 76% based on the final prediction. As the object size decreases, the odds of getting a chord decrease. Even at $D = 20$ km, the chance of getting a chord was 44%. The targeting window for the flight was to place the aircraft within 1 km and 1 s of the aim point along the track (due north of New Zealand). We chose a target point on the shadow center line of 2017 July 10 07:49:11 UTC at latitude $-16°.403333$ and east longitude of $184°.960000$ for a nominal flight altitude of 30,000 ft.

5.3. Observations

5.3.1. SOFIA

SOFIA contains a Focal Plane Imager (FPI+) based the Andor iXon DU-888 commercial CCD camera (Pfüller et al. 2018). The FPI+ usually serves as the guide camera for SOFIA, receiving visible wavelengths via the telescope's dichroic tertiary mirror. Many of the FPI+ characteristics that are advantageous for a guide camera (fast readout rates, zero deadtime between frames, high quantum efficiency, and low read noise) are also critical for an occultation camera, where the desired cadence often produces scenarios with low source counts (Pfüller et al. 2016). In this case, given the relative velocity between Arrokoth and the occultation star of 24 km s^{-1}, we planned for a sampling rate of 20 Hz. That rate was intended to detect rings with equivalent widths of ~1 km.

Our S/N estimator predicted that each 0.05 s exposure would have an S/N of 13, assuming an open filter, an occultation star G mag of 15.57 and 4×4 pixel binning (for an effective plate scale of $2''.04$ per spatial element). Our S/N estimate was comparable to the published FPI+ sensitivities (SOFIA Observers Handbook, Figure 5.1), where an S/N of ~50 is expected in a 1 s exposure of a 15.6 *V*-mag star. Unfortunately, the full Moon was fewer than $10°$ away from Arrokoth during the event, and the highly variable background counts became the dominant noise source. In practice, we found that the S/N per time step was between 3.5 and 5. Nevertheless, the SOFIA/FPI+ lightcurve produced the first occultation detection of Arrokoth—a very short grazing chord, though this was not clear until much later.

Based on the final aircraft telemetry, we were 550 m from the target point in latitude and longitude at the target time. The minimum distance from the target point was 1.8 s later at a distance of 330 m. This degree of success in getting to our aim point took considerable skill and effort on the part of the flight crew and demonstrates what SOFIA can achieve despite the lack of tools for this specific purpose. The most difficult requirement levied on the flight was getting to the aim point at the right time. We attempted to get within 1 s and got very close. In the end, the limiting aspect of our deployment was our ability to predict the right place.

We saw no obvious signs of an occultation during the flight on the real-time monitors. The data required very careful photometric extraction because individual images had rather low apparent S/N
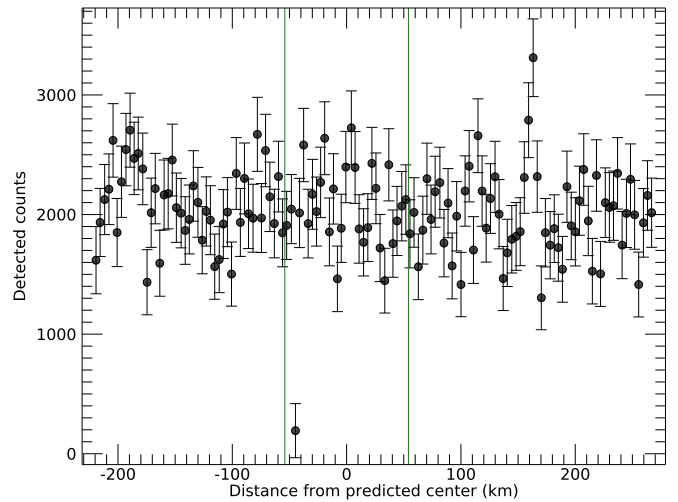
Figure 6. Observations from the 2017 July 10 occultation with SOFIA. The figure shows the lightcurve with a single-point dropout about 45 km prior to the predicted minimum separation. The green vertical lines indicate the predicted 3σ uncertainty limits for the event.

(The data used to create this figure are available.)

on the target star. Figure 6 shows one of the five independent lightcurve reductions. In these data, there is one singularly deep dip in the lightcurve at about 45 km prior to minimum separation. This particular analysis is the result of $2\times$ image binning prior to photometry. We did not apply any spatial shifts to the images and combined the images prior to processing. Because of how the images are indexed, there were two possible binned outcomes. Here we show the outcome that returns the strongest dip. The other option shows a weaker two-point dip. Looking at the original frames prior to combining, the star is missing on the frame at the center of the dip while its flux is reduced somewhat on the frame before and the frame after the center. At our sampling rate, this dip corresponds to a solid-body chord length of ~1 km. We did not immediately identify this dip, but independent processing of the data confirmed the short dropout. Because on-chip reference stars do not show this dip, we believe this to be a real signature associated with Arrokoth. However, we did not complete this analysis until after the third deployment. As far as we knew at the time of the July 17 event, we had come away empty-handed from the first two attempts.

With respect to timekeeping during the flight, we emphasized with both the observing team and flight crew the importance of unambiguous timing information for all images during the occultation sequence. We carried out numerous tests during the outbound flight leg prior to the occultation. We identified and compared four different time sources during the flight: (1) navigation clock used on the flight deck, (2) clock at the science flight control station, (3) GPS-slaved time source used by FPI+ recorded with the science images, and (4) GPS time from an application running on a cell phone with GPS receiver. There was no way to electronically measure the differences between these time sources, and we had to rely on verbal callouts of the clocks to investigate offsets. Past experience with this type of test shows that one can, with care and practice, detect shifts down to about 0.1 s. Clock #4 proved to be unreliable with variable shifts compared to the other three, and we discounted this time source. None of the other three clocks were identical. Clock #1 was 1 s ahead of Clock #2, and Clock #2 was 1 s ahead of Clock #3.
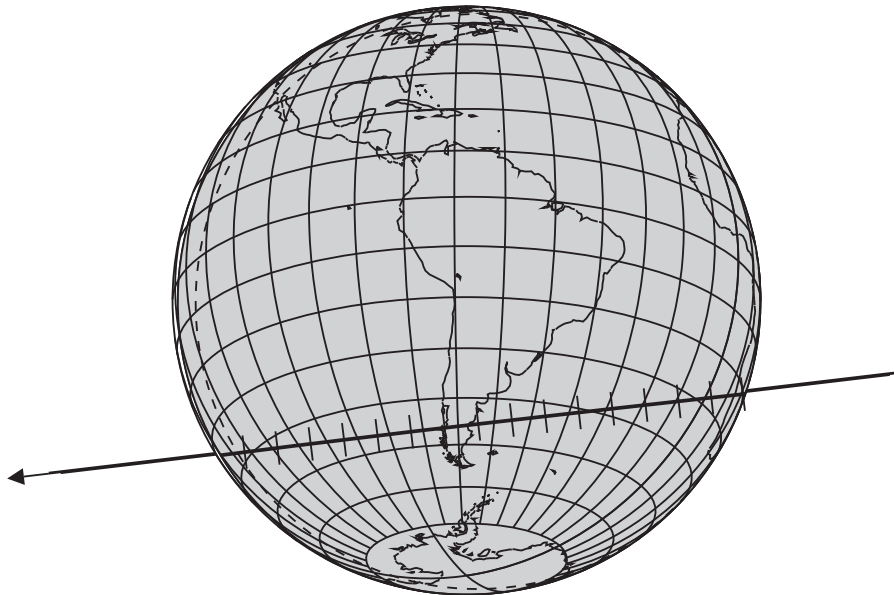
Figure 7. Global view of 2017 July 17 occultation prediction. The figure shows Earth as seen from Arrokoth at the time of geocentric closest approach. The Sun is below the horizon in the regions shaded gray (the entire globe). The dashed line shows where the Sun is at $-12°$ altitude. The solid line indicates the predicted ground track with the width drawn to scale for a 30 km diameter object. The arrowhead indicates the direction of motion, and the ticks are spaced at 30 s intervals from 03:46:00 to 03:53:30 UT. Shadow velocity was 23.5 km s^{-1}. A 46% illuminated Moon was $105°$ from the target at the time of the event.

After careful analysis of the various systems, we concluded that Clock #3 was the one that had been most heavily tested and best understood and were confident that the time tags on the images were correct to within the usual precision limits of a GPS-based system. The targeting of the aim point in time may have been affected by these clock offsets though there was no meaningful degradation of the experiment as a result. A reasonable explanation for the offsets is that Clocks #1 and #2 had (different) out-of-date leap-second almanac information that had never before been recognized because they are not normally tested or relied upon to this level. We had a hard time testing this potential timing concern with the occultation prediction uncertainties at the time. The final postevent reconstructions show that our chosen time reference decision is clearly the most reasonable, giving us additional confidence that the FPI+ timing is correct as expected.

5.3.2. Gemini-south

We acquired data with the AC on Gemini and reduced them in a nearly identical fashion to the June 3rd event reduction. However, we used a larger 120×120 binned pixel window to include a reference star in the frame, resulting in a longer mean deadtime of 0.178 s and an effective imaging cadence of 3.6 Hz. We acquired a 45 minute imaging sequence centered on the nominal shadow passage time. The effective photo-metric S/N of the science target was 17. We did not detect any occultation event in the Gemini data. We computed minimum detectable size limits as done in Section 4.6. Due to the increased deadtime and lower S/N for this sequence, we found a larger minimum detectable size of 5.39 km.

5.3.3. SOAR

We took data remotely at the SOAR telescope on Cerro Pachón using a Raptor photonics Merlin EM247 frame-transfer CCD camera. The Raptor Merlin is a 658×496 pixel CCD camera with 10 μm pixels spanning a relatively narrow $\sim 60''$ by $60''$ FOV on the SOAR 4.1 m telescope. The Raptor includes GPS-based timing. We took images continuously through an open filter wheel at a cadence of 500 ms per image from UT 2017 July 10 06:53:39 to 2017 July 10 08:45:39, and the S/Ns near the middle of the observation window was 26. This station was 2310 km from the shadow center line. No solid-body, rings, or diffuse occulting structures were seen in the data.

5.3.4. Infrared Telescope Facility (IRTF)

Although the 3.0 m NASA IRTF (Mauna Kea, HI) was not near the center line of the occultation prediction, we observed from here to look for extended rings or moons in the vicinity of Arrokoth. S. Benecchi with assistance from S. J. Bus and A. Zangari took data remotely. We used the MIT Optical Rapid Imaging System (MORIS), an Andor iXonEM+ DU-897 camera co-mounted with SpeX (which we did not use) in conventional readout mode. We operated without a filter to get the scale of $0''.11$ and a field of view of $1'$ square (Gulbis et al. 2011). Our exposure time was 0.5 s, and we collected 3000 images over 49.4 minutes from 2017 July 10 07:16:50 until 18 minutes past the predicted occultation time (UT 7:47). We stopped collecting data when clouds claimed the sky, obstructing the field. The seeing was $0''.8$ and S/N on the occultation star in a single exposure was about 4. Analysis of the lightcurve does not show any extended structures around Arrokoth.

6. 2017 July 17 Event

This star was the brightest of the three candidates for 2017. We could observe it from the ground in southern South America (see Figure 7). A deployment for SOFIA was ruled out because it required an extremely long double-length flight path. In the end, we concentrated all of our resources into a mobile deployment from a single location. We ruled out a deployment to Chile because of the weather prospects at that

latitude. We determined that Southern Argentina was the most promising location even though we were not certain we would have clear conditions. Climatic indications for the area indicated a ~50% chance of workable conditions, good enough for the attempt.

6.1. Prediction

We based the final ground track prediction on the same ephemeris used for the July 10 event. Our uncertainty estimates gave a 1σ cross-track error of 14.2 km (0.46 mas) and a timing error of 0.88 s (0.70 mas). These uncertainties were higher than for July 10, due to a larger uncertainty in the star position from *Gaia* DR2 (Gaia Collaboration et al. 2018). Even so, this prediction was three times better than that for June 3, permitting us to deploy ground stations with smaller spacing. As a precaution against a miss as on June 3, instead of deploying to an extremely tight spacing between stations, the deployment plan covered just over 4σ in cross-track spacing relative to the prediction, with a mean spacing between sites of 4 km. Unlike the June event, this coverage and spacing was sufficient for all plausible albedos.

6.2. Deployment

We chose Comodoro Rivadavia to be the central base for the deployment based on local resources, commercial air carrier access, proximity to a major road for transporting the equipment, and proximity to the predicted ground track. At the time this choice was made, the ground track was still uncertain by 200–300 km. The equipment that was used in South Africa was sent via air freight directly to Buenos Aires where it was recombined with the equipment used in Mendoza in June. Everything was then trucked down to Comodoro Rivadavia and distributed to the teams and their vehicles.

We built our deployment pattern around a four-day schedule of events similar to the June 3 deployment. The first night all the teams gathered at the same location in town to test the equipment. The first night provided all teams with an opportunity to practice with the system with other teams nearby. This was particularly useful to troubleshoot difficulties, especially for those new to the telescopes. We split the large group into four subgroups for the second night and sent them to different nearby locations to practice a deployment with less help available. We treated the third night as a dress rehearsal, choosing site locations as if they were actual locations. This strategy provided us with an opportunity to test both the site choices and the teams as if it were the actual event night. The fourth night was the event night. Incredibly, all four nights were workable, which allowed us every opportunity for practice and event-night observations.

This deployment was not without challenges. We had very few roads to work with and our mobility was highly constrained. This forced most teams to work rather close to National Route 3 (RN3), the major north–south highway along the coast. Stray light from passing vehicle headlights caused significant time-variable glare on the images during data collection. Also, this region of Argentina is well known for its generally windy conditions. Indeed, one of the nicknames for Comodoro Rivadavia is the "Capital of the Wind." The conditions started out very calm on the first night but the wind gradually grew in strength with each passing night. The consensus among the teams after the third night was that stray light and telescope shaking from the wind would create serious problems for the event night. The National

University of Patagonia, Comodoro Rivadavia campus (Prof. Marquez), and the mayor's office offered an amazing amount of help with our difficulties. We received help from Prof. Marquez in designing and building windbreaks to shield the telescopes from the winds. The mayor also offered to provide large trucks as windbreaks. We tested all of these on the dress rehearsal night and found these made significant improvements in the data quality. The mayor and the University suggested shutting down RN3 during the time of our observations to address the stray-light problem. Local authorities enforced a two-hour cessation of all traffic movement through the area where we had deployed telescopes. This level of help was absolutely essential to the success of our efforts on event night.

Table 4 provides the final deployment locations. We recorded all of the positions from cell phone-based GPS applications and later confirmed these measurements with Google Earth. We experienced some variation in sky background signal among teams but variation in image motion due to wind dwarfed the variation in sky background signal. Despite the wind mitigation efforts, the wind affected all sites, though it affected some much more strongly than others. Those sites with high levels of wind shake had strongly varying image quality. In the end, this wind shake made the data reductions more difficult but not impossible. Note that the seeing values tabulated are really just an indication of the image quality for normal quality images and the occasional large smearing from wind is not particularly evident from the mean seeing tabulated.

6.3. Observations

Twenty-two of the twenty-four stations were successful in collecting useful data on the target star around the time of minimum separation. Table 4 provides a summary of the data quality and notes for the mobile stations. The Moon was 46% illuminated and 105° away. All stations used a 0.2 s exposure time. We ran all observations for 45 minutes centered on the local predicted event midtime. As with the other 2017 events, we designed this range of time to cover the stable region of the estimated Hill sphere for Arrokoth. The T14 entry shows no sky value, and the data were also not processed due to the target star drifting off the detector prior to the occultation and due to nonstandard data collection settings. The T23 entry again shows no sky value due to it being a very different setup and comparison of sky values has no meaning. The T24 system suffered fatal damage to its internal wiring and could not be repaired in time for the event.

6.4. Data Reductions

We processed all the standard systems (T01–T22) data together, similar to the June 3 data. The lightcurves from all stations are shown in Figures 8 and 9. We copied images within ±1 minute of the predicted midtime out of the full data set for processing. There was no measurable need for bias, dark, or flat-field calibration steps, and therefore, we did not apply these types of corrections. However, the raw images contained a low-level horizontal striping pattern. This striping is a feature of the bias pattern inherent in the detector readout and varied from frame to frame. We easily removed the pattern by computing a robust mean for each row and then subtracting that mean. Each image had a large number of stars (~100) from which we generated a frame-by-frame numerical point-spread function (PSF). We then fit the PSF to all the stars by adjusting

Table 4
Mobile Observing Stations and Teams for 2017 July 17

ID	Team	Latitude (deg)	E Longitude (deg)	Elevation (m)	FWHM (pixels)	Sky (counts)	Comments
T01	A. Olsen, M. Dean	−45.918468	−67.606079	181	9.9	1930	
T02	W. Hanna, P. Hughes	−45.780608	−67.701558	337	9.3	1909	
T03	C. Erickson, C. Wiesenborn, M. Camino	−45.838650	−67.838320	384	7.7	1705	
T04	K. Getrost, L. Ferrario	−46.251567	−67.608167	27	5.1	1739	
T05	P. Tamblyn, R. Reaves	−45.710800	−67.360950	47	7.7	1735	
T06	A. Rolfsmeier, T. Finley, C. Navarrete	−45.447329	−67.666419	409	7.5	1759	
T07	S. Porter, B. Dean	−45.964509	−67.572241	23	6.9	1894	
T08	D. Dunham, C. Ferrell, S. Makarchuk	−45.995417	−67.597194	12	7.7	1689	
T09	T. Blank, K. Singer, Y. Kamerbeek	−45.889267	−67.779917	220	9.3	1981	
T10	A. Friedli, D. Josephs	−45.216667	−67.233333	587	5.1	1676	
T11	S. Conard, A. Resnick, P. Vidal	−46.318980	−67.582630	5	6.5	1648	
T12	B. Keeney, A. Chapman	−46.206200	−67.624167	8	6.7	1924	
T13	R. Venable, C. Lisse	−45.651700	−67.645600	481	9.8	1880	
T14	S. Gurovich. S.A. Stern	−45.565300	−67.627500	635	7–12	⋯	drifted off target
T15	J. Moore, A. Lovell	−46.172500	−67.626944	11	6.8	1917	
T16	A. Verbiscer, C. Tsang, A. Daynes, F. Avelleros, G. Rotondo, I. Rotondo	−45.680692	−67.589490	269	9.5	1716	
T17	A. Zangari, C. Carter, P. Hinton, J. Fazio, M. Herrera	−45.529444	−67.618611	610	6.0	1620	
T18	M. Buie, A. Ocampo, V. Saranitik	−45.823877	−67.460720	11	8.2	1964	
T19	J. Dunham, J. Mackie, P. Saizar	−45.484389	−67.633472	472	4.4	1734	
T20	A. Soto, J. Spagnotto, M. Pereyra	−46.104722	−67.628333	7	7.2	1769	
T21	J. Jewell, S. Strabala, A. Heredia	−46.062500	−67.624167	7	6.9	1894	
T23	M. Nelson, J. Skipper	−45.363655	−67.379478	599	4–7	⋯	variable seeing
T24	L. Wasserman, E. Golub, B. Dickason	−45.266111	−67.302500	583	⋯	⋯	telescope failure
T25	M. Skrutskie, S. Henn	−45.307811	−67.329669	589	2.9	1760	

Note. Positions are all referenced to WGS84 datum.

the position and flux. However, we excluded the target star from fitting at this step. From the fit positions, we derived an astrometric solution for each image based on the *Gaia* DR2 star catalog positions (Gaia Collaboration et al. 2016), corrected for proper motion to the epoch of the images. We then used the astrometric solution to compute a pixel location for the target star. At this point, we computed a PSF fit to the target star where the only free parameter was the star flux. We then computed the midtime for each observation from the GPS time and exposure time recorded in the header of each image.

This data processing methodology was quite valuable, particularly for the images with significant image smear due to wind. In these cases, the PSF is arbitrarily complicated—not just a simple linear smear. As long as the PSF fit accurately replicated the smear, it was possible for us to extract a useful target star flux. Taking full advantage of the PSF method required significant manual effort to guide the PSF building and fitting process. We only applied this extra effort as needed to critical images in and around the time of the actual event. Without this extra corrective step, the target star may appear to drop out for a frame or two. We inspected these cases visually and saw a tortuous wind-driven PSF; however, the target star is still visible. For noncritical images, we noted that the star is still visible and a given dropout is not interesting.

6.5. Fixed stations

6.5.1. SOAR

We took data at SOAR using the Raptor Merlin camera described in Section 5.3.3. The occultation star was the brightest star within the field of view because of the smaller field of view of the Raptor camera. As a consequence, we kept the exposure time at 500 ms to accommodate the dim comparison stars available. Observations spanned between 2017 July 17 02:48:35 and 2017 July 17 04:48:34 UTC, and the S/N near the middle of the observation window was 65. We did not see any signatures due to Arrokoth in the data.

6.6. Results

For this event, we obtained five positive occultation detections roughly in the center of the deployed stations. Table 5 lists the measured timings of these events. Figure 10 shows a plot of the combined geometry between the stations and the occultation timings. These observations clearly showed that Arrokoth was more complicated than a simple ellipsoidal object. Our first interpretation of these data was that Arrokoth was a contact binary shape. In the months following the initial data reduction, we began tracking two additional scenarios to explain the outline from this occultation. One extra option was that the occultation happened during a mutual event between two closely orbiting bodies and just look like a contact binary due to projection effects. This scenario received a lot of attention due to its implication for the *New Horizons* flyby: the spacecraft pointing was effectively set to look at the center of mass. With a binary, that point would be in between the two objects and the *New Horizons* spacecraft might see nothing. The last option was simply a very irregular shape. This option had no special implications for the *New Horizons* encounter and received no special attention. Still, the kink in the shape inferred from the T13 and T16 chords would require a degree of nonsphericity not seen in any other objects in this size class and was thus considered to be unlikely all along.
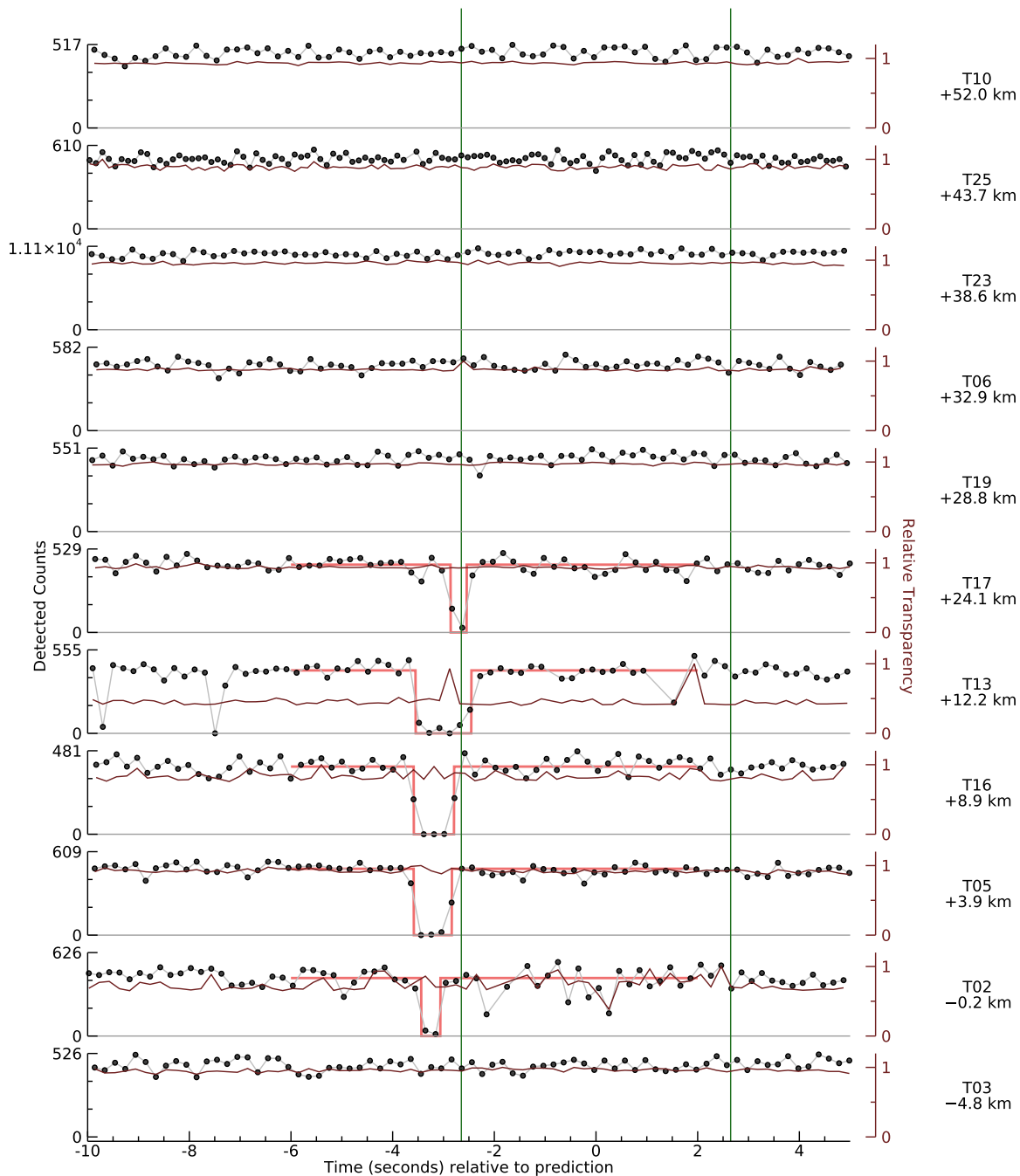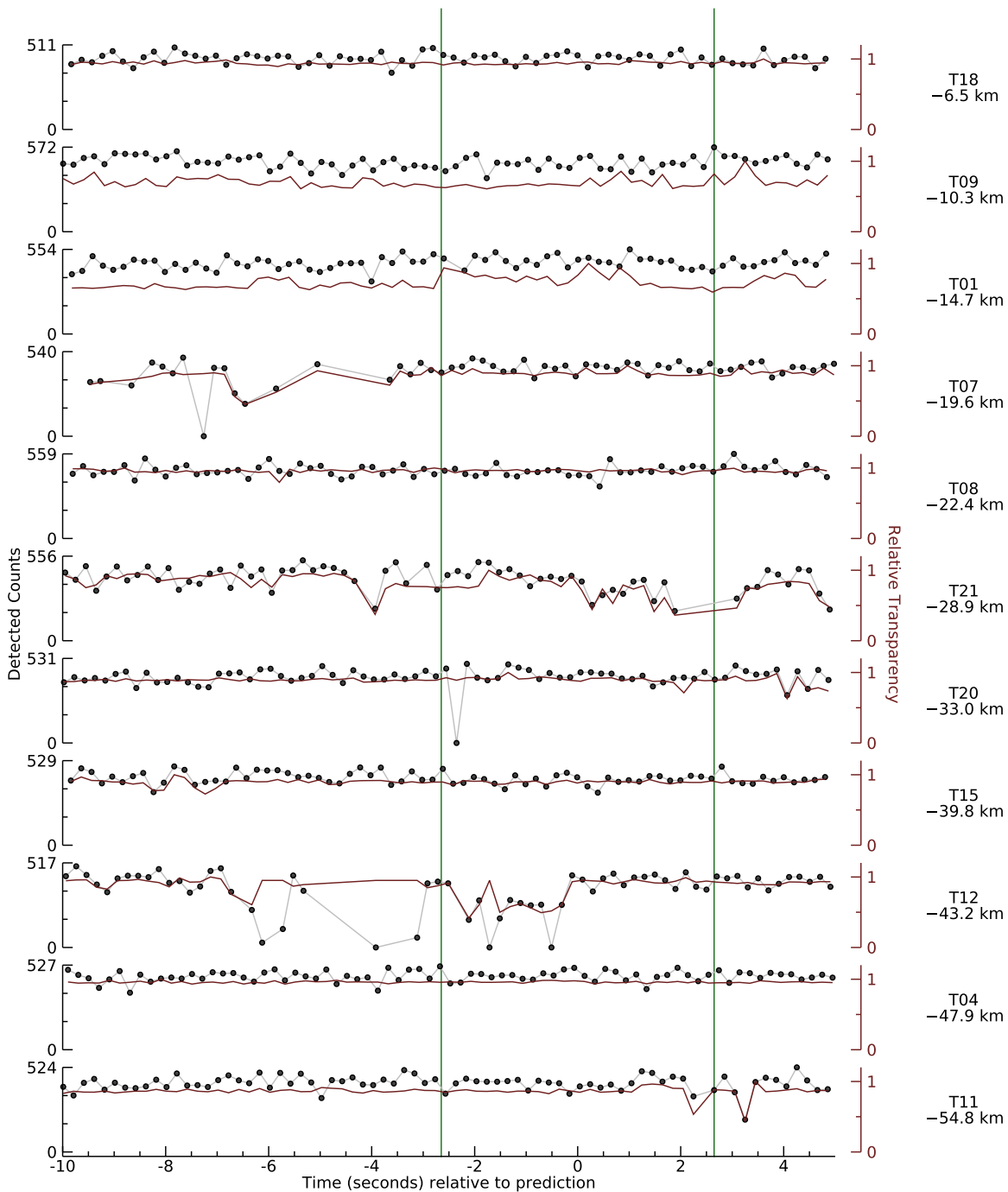
Figure 8. Observations from the 2017 July 17 occultation, part 1. The figure shows the lightcurves from the northern half of the data collected by the mobile stations. Each subplot is labeled on the right with the team number and the cross-track offset. The team numbers are cross-referenced with Table 4. The plots indicate the signal level from each station—higher numbers indicate higher signal levels. The green vertical lines indicate the predicted 3σ uncertainty limits for the event. The second (brown) curve plotted is an estimate of the relative transparency. Five of these curves show an overlaid solid-body model used to extract occultation timings.

(The data used to create this figure are available.)

7. 2018 August 4 Event

Shortly following the success of the 2017 occultations, we searched the *Gaia* catalog (Gaia Collaboration et al. 2016) for additional occultation opportunities in 2018. We identified an event on 2018 August 4 involving a star of magnitude $G = 13.38$. Figure 11 shows the final predicted ground track for this event. We chose to deploy our telescopes to Colombia and Sénégal. Sénégal would be the solitary choice for deployment most times of year as its weather is generally

much drier and more free of clouds. However, this event occurred during their annual rainy season. Climatic considerations indicated a roughly 50% chance of clear skies in either location. However, given the location of the ground track, we expected teams to be much more mobile in Sénégal due to simpler terrain. Thus, we sent 21 of the total 24 systems to Sénégal for the main deployment effort. We sent the other three systems to Colombia along with a few extra QHY cameras to be used on local telescopes.

Figure 9. Observations from the 2017 July 17 occultation, part 2. The figure shows the lightcurves from the southern half of the data collected by the mobile stations. Each subplot is labeled on the right with the team number and the cross-track offset. The team numbers are cross-referenced with Table 4. The plots indicate the signal level from each station—higher numbers indicate higher signal levels. The green vertical lines indicate the predicted 3σ uncertainty limits for the event. The second (brown) curve plotted is an estimate of the relative transparency.

(The data used to create this figure are available.)

7.1. Prediction

The prediction for this event was potentially better than for any of the 2017 occultations. The observational arc was extended by additional *HST* data; further, the successful occultation itself added a new astrometric constraint that was more than an order of magnitude more constraining than any single *HST* observation. The formal uncertainty for the occultation prediction was 13 km cross-track and 1.8 s (36 km) down track. This uncertainty was a

useful guide, provided our assumption of a single body was true. The size shown by the 2017 data was roughly 30×14 km. We had no basis to predict what the projected shape would be in 2018 or what the orientation would be. The prior result could only then suggest the minimum (14 km) or maximum (30 km) cross-track extent. In the case of the binary scenario, the chance of observing during a mutual event a second time was low, and we had to be concerned with the implications of there being two separated
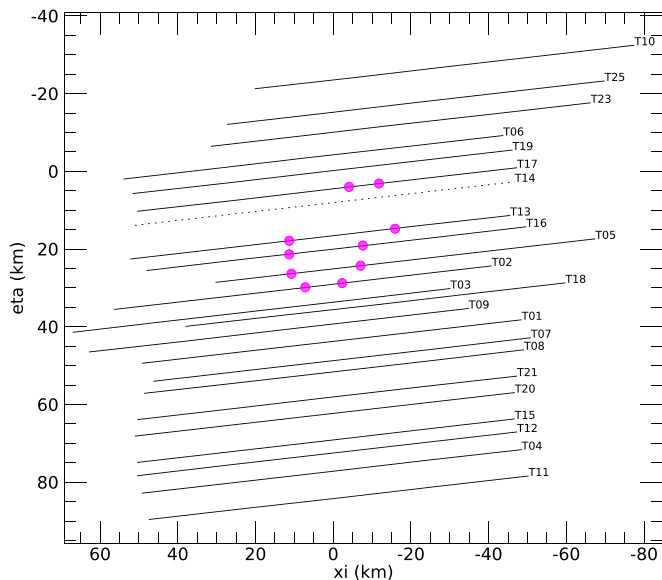
Figure 10. Geometry plot of the 2017 July 17 occultation. Each line shows a track of the topocentric position of Arrokoth relative to the star for 30 s around the time of the event and is labeled with the team number. The stagger between curves is due to the variation on longitude of the observing sites. The magenta dots indicate the interval where we observed the occultations. The one dotted curve did not yield timing information because of mispointing at the time of the event. The team numbers may be cross-referenced with Table 4.

Table 5
Occultation Timings 2018 July 17

Team ID	UT Disappearance	UT Reappearance	Length (km)	Offset (km)
T17	03:50:06.234	03:50:06.551	7.6	24.1
T13	03:50:05.690	03:50:06.785	26.4	12.2
T16	03:50:05.488	03:50:06.283	19.2	8.9
T05	03:50:04.782	03:50:05.530	18.0	3.9
T02	03:50:06.037	03:50:06.412	9.0	−0.2

Note. All times are on 2017 July 17. Offset is relative to the last pre-event prediction.

bodies to cover. With two bodies, we expected diameters between 14 and 20 km requiring tighter coverage. However, there could also be a significant offset between the two bodies relative to the barycenter by tens of kilometers or more. Thus, even though we had an excellent prediction of the center of mass relative to the target star, that knowledge was insufficient to decide on the deployment strategy. Instead, our decisions were driven by what we did not know about Arrokoth, a new regime for stellar occultation predictions and deployments.

7.2. Deployment

Table 6 summarizes the final deployment locations. The goal for all teams was to observe from a location along an assigned line at a fixed distance from the center line and within 500 m of that line. We spaced these tracks at 4 km intervals centered symmetrically around the predicted center line. This spacing would insure two chords on a 10 km body and the number of stations covered almost 120 km in the cross-track direction to better cover the close binary case. The case of the contact

binary would thus be covered by more than 4σ relative to the prediction.

7.2.1. Sénégal

The predicted track was in the northern portion of the country. This area was more thinly populated than the south and also slightly farther from the direction where storms originate. Because the choice for the base camp location was limited, we sent six teams to the Thiès area and the rest deployed from Louga. While splitting the teams made it much harder to tightly coordinate the deployments, our strategy to deploy to a subset of preplanned, fixed, cross-track locations helped.

7.2.2. Colombia

The track was a little north of Bogotá. During the first days, we collected and checked out the equipment and held practice sessions with all local and nonlocal observers. Our mobile teams worked close to the track for dress rehearsal night and event night to avoid excessive driving. The desire was to have sites interleaved with the coverage in Sénégal, but it was difficult to optimize track locations for Colombia because of geographic constraints.

7.3. Observations

On the night of the event in Sénégal, a storm developed and moved northward in the hours just before the observations. The southern sites of the deployment were either rained out or totally clouded out. The weather to the north had local clouds that affected telescope setup and caused strong variability in transparency. We took all data with 0.25 s integration times. Only two sites were unaffected by clouds at the appulse midtime: T08 and T14. The data from T08 show no obvious occultation signal. The data from T14 show a clear dropout of the target star for four consecutive frames.

In Colombia, the dress rehearsal night was successful for setting up and taking practice data. Had the event been this night, these teams would have observed the event. On the actual night of the event, a large storm rolled over the deployment area, preventing any data collection.

7.4. Data Reductions

We reduced the data for these observations in essentially the same way as the 2017 data (see Section 6.4). Figure 12 shows the data from teams whose data could be processed. T08 and T14 provided the two best data sets, and both were straightforward to process, requiring no special treatment.

The T18 data were very challenging. All of the data suffered from extinction due to clouds at roughly 30% of the signal level found at the other two sites. Also, one of the frames during the middle of the occultation happened to be at an instant of a guiding correction or tracking glitch, and the PSF looks like a dumbbell shape. For this case, the automatic tools treated each end of the PSF as a separate source and the resulting stacked PSF was a very poor representation of the image. This problem required a manual edit of the source list to remove the second copy of each source, giving a much better representation of the image PSF. This new PSF was fit to the sources and then a new PSF stack was generated from the improved positions. This
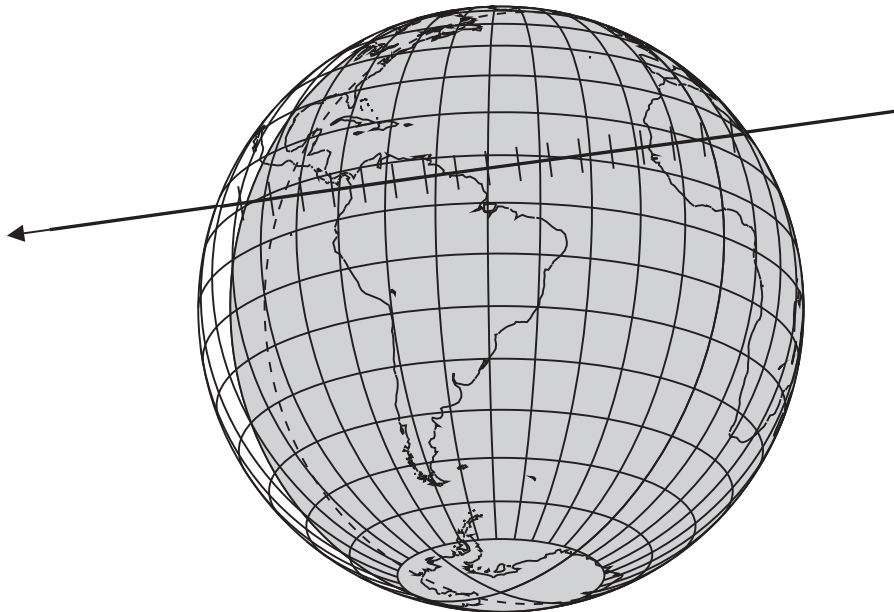
Figure 11. Global view of the 2018 August 4 occultation prediction. The figure shows Earth as seen from Arrokoth at the time of geocentric closest approach. The Sun is below the horizon in the regions shaded gray. The dashed line shows where Sun is at $-12°$ altitude. The solid line indicates the predicted ground track with the width drawn to scale for a 30 km diameter object. The arrowhead indicates the direction of motion and the ticks are spaced at 30 s intervals from 01:20:00 to 01:28:00 UT. Shadow velocity was 21.4 km s^{-1}. A 58% illuminated Moon was 108° away from the target at the time of the event.

second-generation PSF was then fit to the stars and the target as usual.

The extinction suffered by the challenging data sets was nontrivial. For instance, the signal from the target star was usually not even visible in the images. Normal photometric extraction tools that depend on measuring a position and a flux could not retrieve the occultation signal. However, we can compute an accurate location for the star with our astrometric knowledge of the image and the image positions of catalog stars. This computed position enables us to retrieve the flux with a constrained fit that treats the location as a given. The T18 data have a distinctive set of consecutive images where the fitted flux was consistent with zero, indicating an event. The temporal coincidence between T14 and T18 gives us high confidence that the measurements from T18 do, in fact, represent measurements of the limb of the object. The constraints provided by the data from T01, T07, T16, and T17 are minimal, but also not likely to be important given the miss recorded by T08.

7.5. Results

We obtained two positive occultation detections and one unambiguous miss for this event. Figure 12 shows the useful data from the campaign. Table 7 lists the measured timings of the two chords. From this we see that the cross-track offset is comparable to the size of the object and is consistent with the uncertainty of the prediction (13 km). The miss was useful to rule out a second object at the location probed by T08, 14 km north of the predicted center line. However, this constraint was weaker than the implication of getting the successful occultation observations so close to the predicted position. Additionally, both chord lengths are longer than the minimum dimension seen in 2017. These data had to have hit the larger lobe or body. With the continued improvements in the orbit estimate of Arrokoth, the contact binary scenario was really considered to be a formal, but not likely, possibility. For the

binary case, the cross-track offset would imply that the position angle of the system was along the track and yet we did not see a second object. In the end, explaining both the 2017 and 2018 data with a binary system required many special and unlikely circumstances and thus the contact binary option was recognized as the more likely explanation. A more quantitative analysis of the data would have been interesting but there was no time to do so before *New Horizons* arrived at the target and definitively showed the object to be a contact binary (Stern et al. 2019).

7.6. Astrometry

A very powerful result of any successful occultation is in constraining the position of the object relative to the occulted star. This constraint is in physical (i.e., kilometer) scale units and can easily be as good as 1 km or better. Because the scale (km arcsec^{-1}) increases linearly with distance, these positional constraints are especially tight in angular quantities. For instance, at the time of the July 17 event, 1 km was equivalent to 32 μas. Before the release of the *Gaia* DR2 catalog, this information was of little use as the positions of the stars were not very well known. We can see from the values given in Table 1 that the position of the July 17 star was good to about 5–6 km. Even with *Gaia* DR2, astrometry that is derived from a measured occultation position at this distance is limited by the catalog.

Given that our occultation-derived astrometry was limited by the catalog, we did not put special effort into extracting an optimized position for Arrokoth. Prior to the *New Horizons* encounter, we took our reference position from the center of the observed chords that were the closest to the center of the body.

For the July 17 observation, we used the center of the longest chord from station T13 and the coordinate of the occultation star (given in Table 1) from the topocentric location for site T13 (given in Table 4) at the midtime between disappearance and reappearance (Table 5). This derived time is thus 2017 July

Table 6
Observing Stations and Teams for 2018 August 4

ID	Team	Latitude (deg)	E Longitude (deg)	Elevation (m)	FWHM (pixels)	Sky (counts)	Comments
T01	M. Buie, M. Kaire, A. Dieng	+15.621668	−16.246225	50	3.7	1950	some data, high extinction
T02	D. Dunham, C. Carter, L. Sow	+15.663333	−16.258917	36	6.1	1983	no tracking and high extinction
T03	J.-L. Dauvergne, R. Smith, O. Diouf	+15.363200	−16.420182	30	⋯	⋯	no data
T04	B. Keeney, T. Legault, O. Bathiery	+15.234900	−16.085017	44	⋯	⋯	no data
T05	A. Rolfsmeier, C. Ferrell, A. Traore	+15.764722	−16.259167	16	3.0	1634	high extinction
T06	J. Keller, T. Finley, C. Bop	+15.323632	−16.259835	41	5.8	1861	high extinction
T07	F. Colas, M. Grusin, S. Mbaye	+15.710556	−16.268611	50	4.2	1758	some data, high extinction
T08	W. Hanna, R. Ballet, B. Diop	+15.554953	−16.294078	41	3.5	1751	good data
T09	C. Olkin, J. Jewell, S. Gueye	+15.414722	−16.413889	46	⋯	⋯	no data
T10	J. Desmars, I. Smith, D. Diakhite	+15.100417	−16.053806	34	⋯	⋯	no data
T11	S. Porter, S. Moss, D. Ndiaye	+15.186048	−16.083462	50	⋯	⋯	no data
T12	J. Regester, A. Ocampo, G. Faye, B. Yanni	+15.141700	−16.073083	40	⋯	⋯	no data
T13	C. Birnbaum, J. Salmon, D. Dieng	+15.013611	−16.012222	40	⋯	⋯	no data
T14	P. Tamblyn, A. Resnick, I. Gueye	+15.155167	−16.609417	41	4.7	1954	good data
T15	J. Turner, J. Samaniego, L. Toure	+15.818180	−16.245810	20	5.1	2000	no tracking
T16	A. Verbiscer, J. Mackie, M. Faye	+15.871544	−16.236944	17	3.6	1831	some data, high extinction
T17	L. Wasserman, D. Baratoux, M. Ndiaye	+15.914017	−16.261633	10	3.4	1963	some data, high extinction
T18	A. Zangari, J. Dunham, M. Camara	+15.086944	−16.665194	44	4.8	1791	usable data, moderate extinction
T19	P. Hinton, S. Tower, G. Dorego	+15.051117	−16.040150	50	⋯	⋯	no data
T20	R. Leiva, T. Blank	+06.002778	−74.556944	146	⋯	⋯	no data
T21	A. Olsen, K. Nowicki, D. Rojas	+05.909444	−74.560556	173	⋯	⋯	no data
T22	H. Throop, K. Getrost	+06.147778	−74.611944	138	⋯	⋯	no data
T23	B. Andersen, M. Mbaye, A. Ba	+15.271792	−16.536416	37	2.4	1872	no useful data
T24	M. Skrutskie, P. Edwards, M. Dieng	+15.491630	−16.331110	45	1.5	2260	no data
X1	J. Castro, L. Wu, M. Gaviria	+6.296111	−75.330000	2190	⋯	⋯	no data
X2	J. Zuluaga, J. Galvez, M. Ruiz, A. Torres, Y. Roman, P. Cuartas, J. Suazo, L. Ocampo	+6.244722	−75.551389	1671	⋯	⋯	no data
X3	A. Vicini, A. Molina, K. Londoño	+6.051667	−73.85278	1671	⋯	⋯	no data
X4	A. Caycedo, N. Caycedo, G. Gonzlez, F. Moreno, F. Tamayo, K. Sepulveda, F. Tamayo	+6.002222	−73.5552787	1735	⋯	⋯	no data
X5	R. Joya, C. Triana, L. Manzano	+5.827500	−73.607222	1912	⋯	⋯	no data
X6	G. Pinzón, H. Rojas, S. Vanegas, S. Silva, D. Rojas	+5.912222	−73.526389	1753	⋯	⋯	no data
⋯	E. Torres, M. Arango, D. Rondón Fernández, M. Guarn	+6.267894	−75.566125	1490	⋯	⋯	no data

Note. Positions are all referenced to WGS84 datum.

17 03:50:06.238 UT. The result for the August 4 event is not quite as good because we only have two chords, but even here the uncertainty in the star position dominates. As before, we used the position of the star to define the location of the object as seen from the T14 site (longest chord) at the midtime of the event, 2018 August 4 01:21:30.650 UT (see Table 7 for disappearance and reappearance times).

With the then assumption and now knowledge of a single body, these occultation-based positions provided an exceptionally strong constraint on the mean motion of Arrokoth, or equivalently, the semimajor axis of its orbit. This result gave us the most important piece of information needed for a successful spacecraft encounter and that is the heliocentric distance. This constraint also helped to better separate out bad astrometry from the *HST* data set. The consequences of this improvement are discussed in the next section as well as final astrometry that takes advantage of the post-encounter shape model for Arrokoth.

7.7. Combining Event Constraints

A key component of this effort was to provide an orbit estimate for the navigation of *New Horizons* in preparation for its encounter with Arrokoth on 2019 January 1 (Stern et al. 2019). The preocculation predictions and the postobservation reconstructed ground tracks demonstrate the evolution of this preparation. The first four rows of Table 8 provide a summary that shows the final pre-event prediction uncertainties for each occultation campaign. In this case, the improvement is due to each updated orbit estimate. We experienced the largest improvement between the 2017 June and July events because the *HST* lightcurve campaign added a substantial amount of astrometry just prior to the events. Starting in July 2017, each of our successful occultation observations, with their much higher precision positional measurements, also improved the orbit estimate. The final four rows of Table 8 show the formal uncertainties of the reconstructed postdictions using all of the
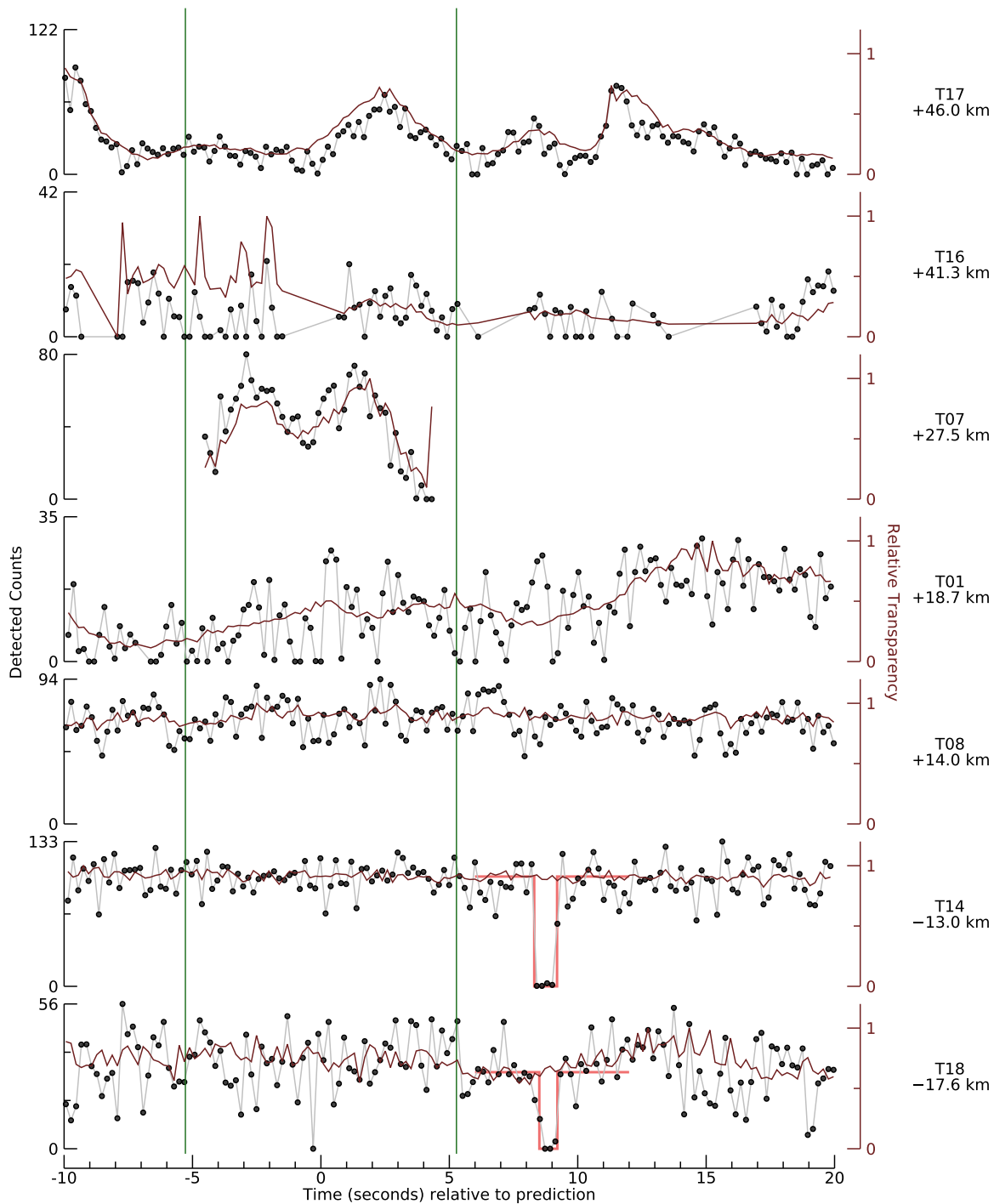
Figure 12. Observations from the 2018 August 4 occultation. The figure shows the lightcurves collected by the mobile stations. Each subplot is labeled on the right with the team number and the cross-track offset. The team numbers may be cross-referenced with Table 6. The plots indicate the signal level from each station—higher numbers indicate higher signal levels. The green vertical lines indicate the predicted 3σ uncertainty limits for the event. The second (brown) curve plotted is an estimate of the relative transparency. Two of these curves show an overlaid solid-body model used to extract occultation timings.

(The data used to create this figure are available.)

HST and occultation data as well as the orbit estimate delivered to the *New Horizons* project.

The orbit ID "may25a" refers to the orbit based on all *HST* data up through and including data taken on 2017 May 25. This was the final orbit solution prior to the first observing campaign. "May25a" was based on 83 good observations providing a total astrometric arc of almost three years. This was

our first orbit reduced against the *Gaia* DR2 catalog (first prerelease version). The orbit with ID "lc1" was the first to include all of the *HST* lightcurve campaign data and was used to target SOFIA for its flight. This version was based on 187 *HST* data points. Subsequent work in the next couple of days led to improved bad-point filtering largely driven by the requirement that the photometry associated with the astrometry

Table 7
Occultation Timings: 2017 August 4

Team ID	UT Disappearance	UT Reappearance	Length (km)	Offset (km)
T14	01:21:30.206	01:21:31.094	19.0	−13.0
T18	01:21:30.604	01:21:31.308	15.1	−17.6

Note. All times are on 2018 August 4. Offset is relative to the last pre-event prediction.

must all be consistent rather than filtering based on astrometric residuals alone. This led to the orbit denoted "lc1gr" based on 197 data points which was used to target the third occultation campaign. The marked reduction in the prediction errors was crucial to the success of the July 17 effort. The orbit with ID "ey3jul1" included numerous improvements in data reduction and new observations. This orbit was based on 230 observations from *HST* up through 2018 July 1 and included the 2017 July 17 occultation measurement. The final *Gaia* DR2 release (Gaia Collaboration et al. 2018) further improved the orbit along with a new pipeline image product from STScI that eliminated trails in the images that can strongly affect measurements of all sources, especially those on the faint end of the detectable range. We discovered these "flc" image products as an unanticipated bonus during a data processing detour working on astrometric measurements of 1I/'Oumuamua (Micheli et al. 2018). The 'Oumuamua observations exhibited faint S/N levels comparable to those seen with Arrokoth but with very different geometric circumstances. This overlapping effort lead to a few more improvements in astrometric processing of the *HST* data. The "ey3jul1" orbit has the smallest range uncertainty of those shown in Table 8.

The final orbit ID "ey7" was the last orbit provided to *New Horizons* for navigation support that did not include any *New Horizons* data. This orbit was based on 195 *HST* observations and two occultations, MU20170717 and MU20180804. The overall improvement for postdictions for all events is evident. Timing and cross-track uncertainties are significantly smaller in all cases. Although the range uncertainty is larger than was computed for the MU20180804 prediction, we consider it more reliable due to the two high-precision occultation constraints separated by slightly more than a year.

Data from four occultation campaigns provided very powerful constraints for both the nature of Arrokoth and its orbit—both clearly of concern for the *New Horizons* encounter. The simplest and most likely explanation for the occultation data throughout most data analysis efforts was a contact binary. However, mission constraints pushed the analysis even further to quantify those scenarios that could not be firmly ruled out. This led to a parallel track of interpretations: Arrokoth could have been either a pair of objects orbiting a mutual center of gravity or a single object with a strange shape. Without a mutual orbit for a putative pair, we needed to pursue heliocentric orbit estimates without constraints from the occultations. Doing so made the *HST*-only orbit estimates robust against the interpretation of the nature of the object but at a significant increase in the uncertainty of the resultant fit. Had the signal level of the Arrokoth images from *HST* been a little higher, it is unlikely these issues would have surfaced. However, the low signal level meant the orbit fit was uncomfortably dependent on the bad-point editing and weighting applied during the orbit fitting process. If Arrokoth were double,

we expected to see strong signatures of barycentric offsets in the occultation-derived positions. We could not completely rule out a binary with just the MU20170717 event. The MU20180804 event indicated that the binary case was far less likely because that event happened at the right cross-track position for a single-object scenario. The larger than anticipated time shift for the MU20180804 event is entirely consistent with a scenario where the second occultation provides a much better determination of the semimajor axis, especially as the interpretation of the other two events, MU20170603 (miss) and MU20170710 (graze), were also still completely consistent with the conclusions. By leaving out the occultation constraints, the four occultation data sets (detections *and* nondetection) were much harder to explain. In the end, the inclusion of two occultation points led to the removal of some data that were having a systematic erroneous effect on the orbit solution.

This analysis also helped us understand the reference systems used for astrometry and orbit analysis. We were concerned about unrecognized systematics between "ground-based" data and spacecraft navigation (radio tracking and optical navigation). This concern often leads to significant underweighting of ground-based priors and places higher demands on the spacecraft navigation data, leading to more conservative uncertainty estimates for spacecraft encounters. For *New Horizons*, we had very little time to observe Arrokoth with spacecraft instruments prior to encounter, and consequently, these priors became unusually important. In particular, the constraint on the heliocentric distance of Arrokoth was dominated by the orbit estimate based on *HST* and occultation data and could not be independently derived from optical navigation until it was too late to use the information. One element of the cross-comparison centered on whether the ICRF was the same for the astrometric support catalog used for ground-based measurements as the ICRF used for spacecraft navigation. The *Gaia* mission team's attention to this issue (Lindegren et al. 2018) was very important to how the *New Horizons* mission used our orbit fitting results. Even so, we used very conservative estimates of the time-of-flight uncertainties for the encounter planning. However, this process indicates that for future missions, the *Gaia* ICRF is close enough to that used for radio tracking to allow treating them as indistinguishable. While this does not lessen the need for care with the measurements themselves, the concern for this particular systematic error has been eliminated through the use of a common reference system.

The four occultation observations also provide important constraints on the spin state of Arrokoth. While we have not completed the shape-model analysis, we can use the preliminary analysis to demonstrate how the encounter observations can be linked to the occultation results. The *New Horizons* imaging data alone are sufficient to fit a shape model with a spin state (pole and rotation period). The current best estimate is a J2000 pole direction of (311°, −42°) and a spin period of 15.92 ± 0.02 hr (Stern et al. 2019). We can use this model and any period consistent with the estimate to render Arrokoth on the plane of the sky as seen from Earth at the time of each occultation. The occultation data from July 17 provide an unambiguous orientation of Arrokoth at that time. Within ±0.06 hr of the nominal period, there are seven discrete periods that match the orientation on July 17 equally well, differing by a single full rotation between the occultation and encounter for adjacent period options. The nominal period implies 803.3

Table 8
Pre- and Postfit Event Uncertainties

Event	Orbit ID	Arrokoth Uncertainty Only					Total Uncertainty				
		Timing		Cross-track		Range	Timing		Cross-track		Range
		(sec)	(mas)	(km)	(mas)	(km)	(sec)	(mas)	(km)	(mas)	(km)
MU20170603	may25a	3.326	2.171	44.455	1.443	2399.21	3.327	2.172	44.614	1.449	2399.24
MU20170710	lc1	0.969	0.778	15.365	0.501	3799.72	0.975	0.783	16.160	0.527	3799.72
MU20170717	lc1gr	0.874	0.690	12.879	0.420	2175.72	0.883	0.697	14.246	0.464	2175.74
MU20180804	ey3jul1	1.748	1.224	12.345	0.402	1427.05	1.759	1.232	13.032	0.424	1427.05
MU20170603	ey7	1.315	0.858	4.899	0.159	1661.76	1.333	0.870	6.567	0.213	1661.76
MU20170710	ey7	0.251	0.201	4.446	0.145	1679.80	0.318	0.255	6.509	0.212	1679.80
MU20170717	ey7	0.221	0.175	4.380	0.143	1683.10	0.316	0.249	6.716	0.219	1683.10
MU20180804	ey7	0.196	0.138	4.014	0.131	1877.90	0.274	0.193	5.772	0.188	1877.90

Note. Orbit IDs are described in the text. Uncertainties are all 1σ.

rotations over this time; thus, periods that match within ± 3 rotations of this case are all possible. For these seven possibilities, we can then look to the orientation at the time of the other events. The June 3 event mostly rules out any option where the major axis of Arrokoth is perpendicular to the shadow track, but this is a weak constraint. Similarly, the July 10 SOFIA data can be used to rank the likelihood of each option, but again, the constraint is weak. The last event from 2018 with the two chords gives the strongest constraint. For this example case, the only period that provides a plausible match for the two chords from 2018 is a period of 15.9380 hr. Assuming the rotation is located to within $10°$ by the July 17 data, the period would then be good to roughly 0.0005 hr, an improvement of a factor of 100. The full analysis is left for future work that will fully integrate the encounter imaging with the occultation profiles.

Figure 13 shows an example of how the current shape model matches the occultation data using this updated period. In this figure are shown views of Arrokoth based on the shape model from Stern et al. (2019) and projected to the time and location of the occultation observation. The dates for each view are indicated in each subpanel. The projected scale is given for a sky-plane view of the object in the J2000 coordinate system. The field of view of each rendered view is about 2 mas. Relevant observations for each event are shown by the colored lines. Nondetections do not intersect the body and are shown in red. The other lines (green and yellow) are for sites recording an occultation. The green lines are a special marker to indicate the reference chord that was used for astrometry (described in Section 7.6). In the case of the 2017 July 10 data, there are two options to match the detection with the body and shown with dashed and solid lines. The solid line is the most likely based on the current orbit of Arrokoth and the *Gaia* DR2 position of the star. Note that the star position uncertainties are all about 4 km in the frame of reference shown in this figure.

We used the shape model as shown in Figure 13 to derive final astrometry from all occultations except for the first where the object was not detected. In the case of the SOFIA event, we provide astrometry for both options shown in the figure for completeness but the option where we clip the southern projected end of the body is preferred. The preference is driven by the better match to the shape model. The southern end of the model (plane-of-the-sky coordinates) comes almost to a point, making it easier to get the short chord duration seen by SOFIA. On the northern end, there is a flat facet at that location that

appears to preclude getting such a short chord. A more detailed shape analysis combining spacecraft imaging data with the occultation constraints may be able to reveal the correct interpretation.

These rendered images were converted to silhouettes, preserving the orientation as shown in Figure 13. We do not know the mass distribution within Arrokoth but we derived an approximate location of the center of mass by finding the area-weighted center of the silhouettes. Any error made with this approximation is significantly smaller than the uncertainty in the star positions. The position of the center is noted with respect to the center of the closest positive chord. The inferred astrometric positions are given in Table 9 along with the topocentric location for each of the measurements.

8. Discussion

The results from this occultation-based effort brings this method to an entirely new level. Two key technological advances and one programmatic approach were crucial to our success. First and foremost, the *Gaia* astrometric catalog precision has lived up to expectations and as a result, opened the door to the study of the outer solar system through occultations. It is now possible to predict occultations well in advance of the event to permit large-scale targeted experiments on small and distant objects. Based on our Arrokoth experience, occultations of trans-Neptunian objects (TNOs) down to a diameter of 10–20 km can be pursued, with weather being the only uncontrollable risk factor that stands in the way of success.

The second key technological advance is, at long last, the availability of the perfect occultation camera. The QHY174M-GPS is a perfect balance of cost, build quality, and capability that combines rigorous timing accuracy with a fast and sensitive detector. The use of sCMOS technology eliminates the need for a shutter and minimizes deadtime. While there are even faster sCMOS-based camera systems, this one is good enough with only ~ 1 ms deadtime per read. The cost of the system is also a fundamentally valuable advantage. These cameras cost a total of $26,400 to outfit all telescopes while the previous generation of frame-transfer CCD systems could be expected to cost $660,000 just for the detector, with extra costs for providing accurate timing. Another element of the systems was the design and cost of our telescopes, again an off-the-shelf commercial product. The 40 cm Skywatcher telescopes are easy to setup and use under the conditions required
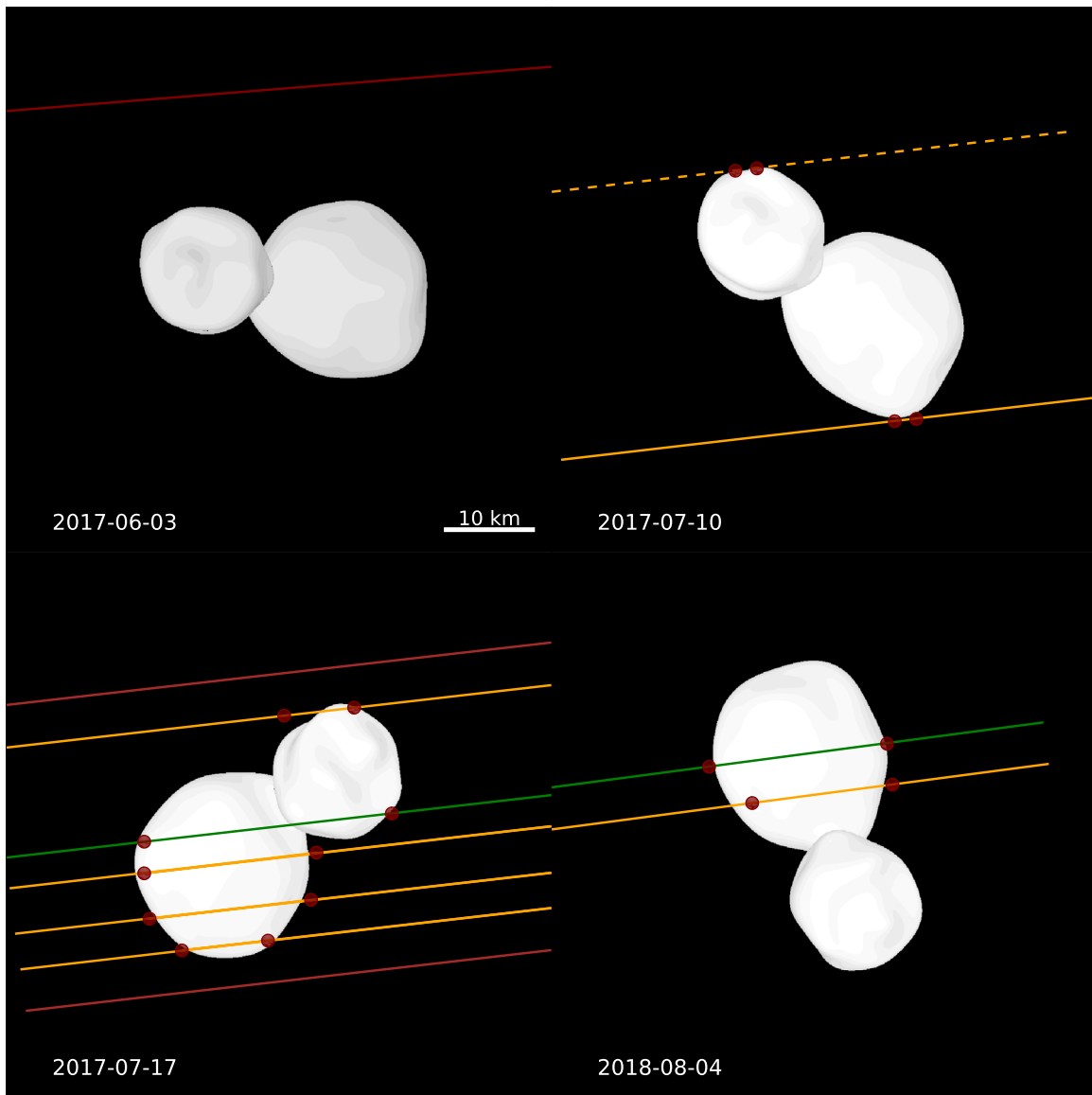
Figure 13. Comparison of shape model with occultation data. The projected shape and orientation of Arrokoth are compared to the occultation data for all four events in a J2000 sky-plane view. Red lines indicate observations that did not record an occultation. Green and yellow lines are those that did. The red dots denote where the star either disappeared or reappeared. The dashed yellow line for 2017 July 10 is an alternate but less favored option.

Table 9
Occultation Astrometry

Site ID	UTC	Latitude (deg)	E Longitude (deg)	Altitude (m)	R.A.	Decl.
SOFIA	2017/07/10 07:49:05.50	−16.387247	+184.961026	12354.8	19:00:41.620047	−20:38:44.53765
T13	2017/07/17 03:50:06.24	−45.651700	−67.645600	481.0	19:00:08.291521	−20:39:37.98218
T18	2018/08/04 01:21:30.96	+15.086944	−16.665194	44.0	19:04:21.478510	−20:35:36.54727
SOFIA*	2017/07/10 07:49:05.50	−16.387247	+184.961026	12354.8	19:00:41.620011	−20:38:44.53676

Note. R.A. and decl. are given in EME2000 coordinates and are topocentric locations. All topocentric locations are referenced to the WGS84 datum. SOFIA* is the alternate, nonpreferred, position for that data set.

of an occultation observation. Our full set of telescopes cost only $74,800, and each is individually cheap enough that complete replacement of a failed system is a viable option.

The capabilities of these systems, combined with their cost, allowed us to consider an entirely new programmatic approach using a large set of mobile equipment. Our occultation deployment did not break any records for the number of involved systems or observers. What was unusual was the size of the team that was deployed as a single coordinated effort and all following the same direction. The operational methodology that emerged through our three large mobile deployments was one of strategic placement of each and every station to optimize

the overall experiment and its chances for success. The level of central coordination was far stronger for our campaigns than has been typical of prior efforts. Our experience shows this to have been an effective strategy and one that is especially important for mapping out the shape of small objects such as Arrokoth. Objects in this size range are particularly well suited to centrally organized deployments.

This project provides an interesting example for the use of the *Gaia* star catalog by providing a homogeneous set of data that are all referenced near catalog epoch star positions. The challenge of both successful occultation observations and the *New Horizons* encounter was met despite the short observational arc on Arrokoth. The full details of the orbit and error determination are discussed in Porter et al. (2018). However, some general lessons learned from that work are worth summarizing here. The event prediction uncertainties provided here are dependent on capturing all sources of noise and proper handling of any priors. The hardest part of this process is capturing or constraining systematic errors. We now see that the missed occultation on our first attempt was clearly the result of such unrecognized systematics. Our best estimate of the source of these early systematics is the filtering applied to reject bad astrometric measurements. Bad-point rejection became easier as our data set increased; however, we lacked sufficient data prior to 2017 June 3 to know for sure which measurements were bad. To check this conjecture, we ran a test case that used the final filtering used for "ey7" but restricted the orbit fit to the data available prior to June 3. Had that prediction been used with the exact deployment strategy from that attempt, we would have been successful. We suspected this was the case at the time, but there was little we could do about it. We had insufficient ground-track coverage because of the finite number of sites, the ground-track uncertainty, and our size estimates at the time. Doubling the spread, while possible, would have resulted in spacing that was too coarse. Given available data at the time, it was unlikely we could have obtained a better outcome for June 3. Even so, the June 3 deployment provided an important nondetection constraint as well as other logistical benefits. This first effort was absolutely essential as a full-up field test of this scale of deployment. Without the June 3 event, we would have severely compromised the chances of success for the July 17 campaign.

Our experiences highlight a particularly useful occultation observing strategy. In many cases, particularly with smaller targets, the first occultation is the hardest to get. Trying to get full size and shape information on this first event makes the task even harder by requiring many more stations. Instead of trying to get it all on the first attempt, we can chose to cover an event with relatively sparse coverage with the expected goal being to get just a single chord. This single chord can provide a much higher precision astrometric measurement than can be achieved with the usual direct imaging observations. For instance, one ground-based image can be expected to collect a position good to 50 mas. A successful occultation, even a single-chord data set, can easily get a position good to a factor of 100 better at 0.5 mas. With simple $\sqrt{N}$ scaling, getting a factor of 100 improvement to match would require 10,000 such images. Most of these small TNOs can only be seen with large (4–10 m) telescopes. Sufficient access to these large apertures is not at all likely, and this effort would serve for just one object. A more efficient way to proceed is to break down the occultation work into two components: one to get the first chord with a low-cost deployment strategy (e.g., fixed-site network, possibly robotic) and then follow up with a high-density mobile campaign. It is also important to keep in mind that the high-density campaigns are expensive—comparable to the cost of five nights on one of the Keck Telescopes in Hawaii. Thus, it is well worth every practical effort to make the most of what could be rare major coordinated campaigns unless there is a change in the way large occultation efforts can be funded. So far, this type of deployment has only been possible when it is important for supporting a spacecraft mission.

9. Conclusions

This work represents an unprecedented level of effort across many agencies, projects, and international borders. We carried out a very large centrally organized occultation deployment effort, which resulted in an unprecedented investigation of a small body in the outer solar system. The combination of a new generation of occultation cameras with integrated timing, together with multiple, large, mobile telescopes, supported by the new *Gaia* star catalog, has demonstrated we now have the means to investigate this class of objects more deeply with high spatial density chords.

Our occultation results clearly showed that Arrokoth was a contact binary. A far deeper perspective is added when combined with the results from the *New Horizons* flyby (Stern et al. 2019). With this newfound understanding, future occultations can help answer the question of how unique or typical Arrokoth is, as well as investigating other dynamical classes of objects in the Kuiper Belt. Surveys that work in the thermal infrared can provide some of this context. Only occultations can probe hundreds or thousands of such bodies and provide statistics on the fraction of objects that are tight binaries and contact binaries.

On a practical note, the first occultation of this size of body is always likely to be difficult. Mobile ground deployments are very powerful and the only way to get high-density multichord observations of a specific object, but they are also an expensive undertaking. Any other means by which even a single-chord observation can be collected will lead to a substantial improvement in predictions of subsequent events and serve to make large ground deployments more effective.

This work demonstrates that a new pathway for understanding the Kuiper Belt is now opened. The combination of large mobile occultation deployments, astrometry from large telescopes or *HST*, and the amazing *Gaia* star catalog all combine to enable these investigations and will be limited only by desire and funding.

ORCID iDs

Marc W. Buie ⓘ https://orcid.org/0000-0003-0854-745X
Simon B. Porter ⓘ https://orcid.org/0000-0003-0333-6055
Dirk Terrell ⓘ https://orcid.org/0000-0001-8406-4172
Alex Harrison Parker ⓘ https://orcid.org/0000-0002-6722-0994
David Baratoux ⓘ https://orcid.org/0000-0002-1785-5262
Rodrigo Leiva ⓘ https://orcid.org/0000-0002-6477-1360
Anne J. Verbiscer ⓘ https://orcid.org/0000-0002-3323-9304
Joseph I. Samaniego ⓘ https://orcid.org/0000-0002-5471-4426
Lawrence H. Wasserman ⓘ https://orcid.org/0000-0001-5769-0979
Susan D. Benecchi ⓘ https://orcid.org/0000-0001-8821-5927
Amir Caspi ⓘ https://orcid.org/0000-0001-8702-8273
J. J. Kavelaars ⓘ https://orcid.org/0000-0001-7032-5255
M. F. Skrutskie ⓘ https://orcid.org/0000-0001-8671-5901
Alejandro Soto ⓘ https://orcid.org/0000-0002-2333-0307

Paolo Tanga ⓘ https://orcid.org/0000-0002-2718-997X
Eliot F. Young ⓘ https://orcid.org/0000-0001-8242-1076
Bridget C. Andersen ⓘ https://orcid.org/0000-0001-5908-3152
Amanda S. Bosh ⓘ https://orcid.org/0000-0003-4772-528X
Josselin Desmars ⓘ https://orcid.org/0000-0002-2193-8204
David W. Dunham ⓘ https://orcid.org/0000-0001-7527-4207
Hugo A. Durantini Luca ⓘ https://orcid.org/0000-0002-4143-2550
Nicolas Erasmus ⓘ https://orcid.org/0000-0002-9986-3898
Wesley C. Fraser ⓘ https://orcid.org/0000-0001-6680-6558
Anja Genade ⓘ https://orcid.org/0000-0001-6841-8436
Giovanni Francisco González Murillo ⓘ https://orcid.org/0000-0002-0349-0880
P. C. Hinton ⓘ https://orcid.org/0000-0001-9504-0520
Joshua A. Kammer ⓘ https://orcid.org/0000-0002-3441-3757
Brian A. Keeney ⓘ https://orcid.org/0000-0003-0797-5313
Emily A. Kramer ⓘ https://orcid.org/0000-0003-0457-2519
Stephen E. Levine ⓘ https://orcid.org/0000-0002-1050-3539
Carey M. Lisse ⓘ https://orcid.org/0000-0002-9548-1526
Freddy Moreno ⓘ https://orcid.org/0000-0003-0670-356X
Catherine B. Olkin ⓘ https://orcid.org/0000-0002-5846-716X
Jay M. Pasachoff ⓘ https://orcid.org/0000-0002-4372-4928
Julien Salmon ⓘ https://orcid.org/0000-0002-5977-3724
Pablo Santos-Sanz ⓘ https://orcid.org/0000-0002-1123-983X
Amanda A. Sickafoose ⓘ https://orcid.org/0000-0002-9468-7477
Kelsi N. Singer ⓘ https://orcid.org/0000-0003-3045-8445
Andrew W. Stephens ⓘ https://orcid.org/0000-0002-4434-2307
Henry B. Throop ⓘ https://orcid.org/0000-0002-1988-223X
Constantine C. C. Tsang ⓘ https://orcid.org/0000-0002-1939-6813

Jake D. Turner ⓘ https://orcid.org/0000-0001-7836-1787
Jorge I. Zuluaga ⓘ https://orcid.org/0000-0002-6140-3116

References

Allsman, R. A., Axelrod, T. S. & for the Macho Collaboration 2001, arXiv:astro-ph/0108444
Barry, M. A. T., Gault, D., Bolt, G., et al. 2015, PASA, 32, e014
Benecchi, S. D., Porter, S., Buie, M. W., et al. 2019, Icar, 334, 11
Buie, M. W., Porter, S. B., Verbiscer, A. V. & 9 coauthors 2018, AAS DPS Meeting, 50, 509.06
Coppejans, R., Gulbis, A. A. S., Kotze, M. M., et al. 2011, PASP, 125, 976
Fraser, W. C., Bannister, M. T., Pike, R. E., et al. 2017, NatAs, 1, 0088
Fraser, W. C., Trujillo, C., Stephens, A. W., et al. 2013, ApJL, 774, L18
Gaia Collaboration, Brown, A. G. A., Vallenari, A., et al. 2018, A&A, 616, A1
Gaia Collaboration, Prusti, T., de Bruijne, J. H. J., et al. 2016, A&A, 595, A1
Gulbis, A. A. S., Bus, S. J., Elliot, J. L., et al. 2011, PASP, 123, 461
Gwyn, S. D. J. 2014, JInst, 9, C04003
Lindegren, L., Hernández, J., Bombrun, A., et al. 2018, A&A, 616, A2
Micheli, M., Farnocchia, D., Meech, K. J. & 14 coauthors 2018, Natur, 559, 223
Nesvorný, D., Youdin, A. N., & Richardson, D. C. 2010, AJ, 140, 785
Noll, K. S., Grundy, W. M., Chiang, E. I., Margot, J.-L., & Kern, S. D. 2008, in The Solar System Beyond Neptune, ed. M. A. Barucci et al. (Tucson, AZ: Univ. Arizona Press), 345
Pfüller, E., Wiedemann, M., Wolf, J., & Krabbe, A. 2016, Proc. SPIE, 9908, 99082W
Pfüller, E., Wolf, J., & Wiedemann, M. 2018, JAI, 7, 1840006
Porter, S. B., Buie, M. W., Parker, A. H., et al. 2018, AJ, 156, 20
Stern, S. A., Weaver, H. A., Spencer, J. R., et al. 2019, Sci, 364, eaaw9771
Stern, S. A., Weaver, H. A., Spencer, J. R., & Elliott, H. A. 2018, SSRv, 214, 77
Temi, P., Marcum, P. M., Young, E., et al. 2014, ApJS, 212, 24
Young, E. F., Showalter, M. R., Porter, S. B., et al. 2018, RNAAS, 2, 224
Zacharias, N., Finch, C. T., Girard, T. M., et al. 2013, AJ, 145, 44